

A multiple-time-step integration algorithm for particle-resolved simulation with physical collision time

Zhengping Zhu^a, Ruifeng Hu^b, Xiaojing Zheng^a

^a*Research Center for Applied Mechanics, School of Mechano-Electronic Engineering, Xidian University, Xi'an 710071, China*

^b*Center for Particle-Laden Turbulence, Key Laboratory of Mechanics on Disaster and Environment in Western China, Ministry of Education, and Department of Mechanics, College of Civil Engineering and Mechanics, Lanzhou University, Lanzhou 731000, China*

Abstract

In this paper, we present a multiple-time-step integration algorithm (MTSA) for particle collisions in particle-resolved simulations. Since the time step required for resolving a collision process is much smaller than that for a fluid flow, the computational cost of the traditional soft-sphere model by reducing the time step is quite high in particle-resolved simulations. In one state-of-the-art methodology, collision time is stretched to several times the flow solver time step for the fluid to adapt to the sudden change in particle motion. However, the stretched collision time is not physical, the hydrodynamic force may be severely underestimated during a stretched collision, and the simulation of sediment transport may be sensitive to the stretched collision time. The proposed MTSA adopts different time steps to resolve fluid flow, fluid-particle interaction, and particle collision. We assessed the MTSA for particle-wall collisions as well as particle-particle collisions, determined the optimal iteration number in the algorithm, and obtained excellent agreements with experimental measurements and reference simulations. The computational cost of the MTSA can be reduced to about one order of magnitude less than that using the traditional soft-sphere model with almost the same accuracy. The MTSA was then implemented in a particle-resolved simulation of sediment transport with thousands of particles. By comparing the results obtained using the MTSA and a version of the stretching collision time algorithm similar to [Costa et al. \(2015\)](#), we found that stretching the collision time reduced particle stiffness, weakened particle entrainment, and affected some turbulence and particle statistics.

1. Introduction

Particle-laden two-phase flows are widely encountered in industrial engineering and natural environments (Balachandar and Eaton, 2010; Brandt and Coletti, 2022), such as aeolian sand and dust movement, sediment transport, and fluidized-bed processes. When simulating particle-laden flows, if the flow field surrounding particles is fully resolved, it is called a particle-resolved simulation. A number of different particle-resolved simulation approaches have been developed, like the immersed boundary (IB) method (Mittal and Iaccarino, 2005; Uhlmann, 2005; Luo et al., 2007; Breugem, 2012; Kempe and Fröhlich, 2012b; Zhou and Fan, 2014; Tao et al., 2018; Huang and Tian, 2019; Wang et al., 2019; Verzicco, 2023) and the distributed Lagrange multiplier (DLM)/fictitious domain approach (Glowinski et al., 1999, 2001; Yu and Shao, 2007, 2010; Shao et al., 2012). Particle-resolved simulations have been widely used to obtain high-fidelity simulation data, which is greatly helpful for developing reduced-order models (Bagchi and Balachandar, 2003; Eaton, 2009; Homann et al., 2013; Tenneti and Subramaniam, 2014; Zhou and Fan, 2015; Akiki et al., 2017; Seyed-Ahmadi and Wachs, 2020; Zhang et al., 2020; Wang et al., 2022; Xia et al., 2022a,b) or studying the mechanism of the fluid-particle interactions (Uhlmann, 2008; Kidanemariam and Uhlmann, 2014b; Vreman, 2016; Vowinckel et al., 2016; Luo et al., 2017; Peng et al., 2020; Costa et al., 2021; Yu et al., 2021).

The focus of the present paper is on the collision algorithm for particles in particle-resolved simulations. Particle collision modeling is essential in particle-resolved simulations, whether a particle-laden flow is in the dense regime (Kidanemariam and Uhlmann, 2014b; Vowinckel et al., 2014; Picano et al., 2015) or the dilute regime (Costa et al., 2020). Soft-sphere model (Hertz, 1882; Mindlin and Deresiewicz, 1953) is one of the most popular collision models in particle-resolved simulations when multi-particle contact frequently occurs. However, the traditional soft-sphere model (*i.e.*, the soft-sphere model with physical collision time) can be inefficient when applied to particle-resolved simulations, as the time scale associated with particle collision is typically much smaller than that of fluid flow, particularly for rigid particles. This mismatch can lead to expensive computation if using the same time step to resolve particle collisions and advance fluid flow simultaneously. On the other hand, the stretching collision time algorithm (SCTA) (Feng et al., 2010; Papista et al., 2011; Kempe and Fröhlich, 2012a; Costa et al., 2015; Biegert et al., 2017; Rettinger and Råde, 2022) was proposed as a remedy and has been shown to be successful in reproducing the

particle trajectories of particle-wall (Joseph et al., 2001; Gondret et al., 2002; Joseph and Hunt, 2004) and particle-particle (Yang and Hunt, 2006) collisions. In the SCTA, the collision time T_c was stretched to N times the flow solver time step Δt_f (*i.e.*, $T_c = N\Delta t_f$) since the fluid requires time to adapt to the sudden change in particle velocity during collisions. By stretching the collision time, the computational efficiency can be improved compared with the traditional soft-sphere model. The particle stiffness and damping coefficient are determined by the desired restitution coefficient $e_{n,d}$ and collision time T_c . However, the SCTA can only retain the particle kinematic properties rather than the mechanical properties as it greatly reduces the physical stiffness. Most of the SCTA is based on a linear spring-dashpot system, and the stiffness and damping coefficients were determined by an algebraic expression (Izard et al., 2014; Kidanemariam and Uhlmann, 2014b; Costa et al., 2015; Ardekani et al., 2016). Other implementations are based on the Hertzian contact theory, which is nonlinear, and the stiffness and damping coefficients were determined by an optimization procedure (Kempe and Fröhlich, 2012a; Ray et al., 2015; Biegert et al., 2017). Rettinger and Råde (2022) developed an efficient four-way coupled lattice Boltzmann-discrete element method using the stretching collision time algorithm. They found that the collision time T_c is a critical parameter of the method, which has a significant effect on the collision dynamics. The collision time should be stretched as $T_c = 2.31D_p/c_s$ to allow the fluid to adapt to the sudden change in particle velocity, where D_p is particle diameter and c_s is the lattice speed of sound. Recently, different from the SCTA developed based on the soft-sphere model, Jain et al. (2019) proposed an algorithm based on the hard-sphere model, and the hydrodynamic forces are incorporated during the collision using a semi-implicit IB method (Tschisgale et al., 2018).

Although the SCTA can significantly reduce the computational cost compared with the traditional soft-sphere model and reproduce the experimental results of particle-particle and particle-wall collisions successfully (Joseph et al., 2001; Gondret et al., 2002; Joseph and Hunt, 2004; Yang and Hunt, 2006), it has several significant drawbacks. First, particle stiffness in the SCTA is greatly reduced by stretching the collision time, which is not physical. Second, the artificially stretched collision time T_c should be large enough to get converged trajectory (Rettinger and Råde, 2022). However, the hydrodynamic force during such an artificially long collision process is usually neglected and significantly underestimated, which may lead to erroneous predictions of turbulence statistics (Xia et al., 2020) and can be expected to also

affect particle statistics in massive-particle-laden flows, like sediment transport. To avoid introducing a stretched collision time, [Li et al. \(2020\)](#) were the first to use the physical collision time T_c in particle-resolved simulations. They adopted single non-uniform grid points with $O(10^5)$ grid elements to resolve the particle and lubrication force, yielding excellent agreement with experimental results. However, such an extra-high grid resolution is almost impossible in cases with a large number of particles.

The present study proposed a multiple-time-step integration algorithm (MTSA) to reproduce the experimental results ([Joseph et al., 2001](#); [Gondret et al., 2002](#); [Joseph and Hunt, 2004](#); [Yang and Hunt, 2006](#)) and simulations ([Costa et al., 2015](#)) using the soft-sphere model with physical collision time on a uniformly coarse grid. The grid resolution is about $D_p/\Delta x = O(10)$, where Δx is the grid spacing. To overcome the time scale mismatch problem, three different time steps are employed in the MTSA to resolve fluid flow, fluid-particle interaction and particle motion during particle collisions. The pressure Poisson equation is only solved at the fluid flow time step to reduce computational cost. When time is advanced to the same instant, the fluid and particle information will be updated and synchronized. The MTSA can reduce the computational cost of the traditional soft-sphere model by nearly one order of magnitude and avoids artificially reducing particle stiffness like the SCTA. Meanwhile, we validated the accuracy and convergence of the MTSA with experimental data ([Joseph et al., 2001](#); [Gondret et al., 2002](#); [Joseph and Hunt, 2004](#); [Yang and Hunt, 2006](#)), numerical data ([Costa et al., 2015](#)), and a reference simulation using the traditional soft-sphere model with fine time steps. We also presented guidelines for determining the optimal values of the parameters in the MTSA. The MTSA was then applied to a sediment transport case with thousands of finite-size particles. The results of the MTSA were compared for the first time with those obtained by the SCTA to investigate the effects of particle stiffness in a particle-resolved simulation of sediment transport.

The structure of the paper is arranged as follows. The governing equations and physical models for fluid flow and particle motion are given in §2. In §3, the MTSA is introduced. In §4, the influence of the time substep size is systematically analyzed and discussed in particle-wall and particle-particle collisions to yield a universally optimal time substep size. The MTSA is further applied to a sediment transport case with thousands of finite-size particles, and the effect of particle stiffness is investigated. Finally, we present the main conclusions of the paper in §5.

2. Models

2.1. Governing equations

The particle-laden flow considered here is governed by the Navier-Stokes equations for the carrier phase and the Newton-Euler equations for the dispersed particulate phase. The motion of an incompressible, Newtonian fluid flow is governed by the following continuity and momentum equations:

$$\nabla \cdot \mathbf{u} = 0, \quad (1)$$

$$\frac{\partial \mathbf{u}}{\partial t} = -\nabla \cdot (\mathbf{u}\mathbf{u}) - \frac{1}{\rho_f} \nabla p + \nu_f \nabla^2 \mathbf{u} + \mathbf{f}, \quad (2)$$

where \mathbf{u} is the fluid velocity, p is the pressure, \mathbf{f} is the volume force imposed to take into account the fluid-particle interaction or the IB force, ρ_f is the fluid density, and ν_f is the fluid kinematic viscosity.

The translational and angular velocities of a particle are advanced by solving the Newton-Euler equations, which for a spherical particle are reduced to

$$\rho_p V_p \frac{d\mathbf{u}_p}{dt} = \oint_{\partial V} \boldsymbol{\tau} \cdot \mathbf{n}_p dA + (\rho_p - \rho_f) V_p \mathbf{g} + \mathbf{F}_{p,lub} + \mathbf{F}_{p,col}, \quad (3)$$

$$I_p \frac{d\boldsymbol{\omega}_p}{dt} = \oint_{\partial V} \mathbf{r} \times (\boldsymbol{\tau} \cdot \mathbf{n}_p) dA + \mathbf{T}_{p,col}, \quad (4)$$

where ρ_p is the particle density, V_p is the volume of the particle and equal to $(4/3)\pi R_p^3$ for a sphere with radius R_p ; I_p is the moment of inertia of the particle and equal to $(2/5)\rho_p V_p R_p^2$ for a spherical particle; \mathbf{u}_p and $\boldsymbol{\omega}_p$ are the translational and angular particle velocities, respectively; $\boldsymbol{\tau} = -p\mathbf{I} + \mu_f(\nabla\mathbf{u} + \nabla\mathbf{u}^T)$ is the hydrodynamic stress tensor (the superscript T indicates the transposition of a tensor); μ_f is the fluid dynamic viscosity; \mathbf{n}_p is the outward-pointing unit normal vector at the surface ∂V of the particle; \mathbf{r} is the relative position vector of the particle surface to the particle center; \mathbf{g} is the gravitational acceleration; $\mathbf{F}_{p,lub}$, $\mathbf{F}_{p,col}$, and $\mathbf{T}_{p,col}$ are the total lubrication force, total collision force, and total collision torque acting on the particle p , respectively. The subscript p refers to the quantities of particle p . The carrier and dispersed phases are coupled by the volume force \mathbf{f} , which is calculated by the multidirect forcing IB method (Luo et al., 2007; Breugem, 2012). The governing equations of the carrier phase are discretized on a uniform staggered Cartesian grid, which is referred to as the Eulerian grid.

A particle is discretized by a fixed grid attached to the particle surface, which is referred to as the Lagrangian grid. The quantities between the Eulerian and Lagrangian grid points are transferred through a regularized Dirac delta function δ_d (Roma et al., 1999).

To avoid the difficulty of directly calculating the surface integrals $\oint_{\partial V} \boldsymbol{\tau} \cdot \mathbf{n}_p dA$ and $\oint_{\partial V} \mathbf{r} \times (\boldsymbol{\tau} \cdot \mathbf{n}_p) dA$, these surface integrals are converted into volume integrals by means of a momentum balance over the volume occupied by a particle. The volume force \mathbf{f} is transferred from the Eulerian grid to the Lagrangian grid. Based on the above operations, the equations of particle motion (3) and (4) can be rewritten as (Uhlmann, 2005; Kempe and Fröhlich, 2012b; Breugem, 2012)

$$\rho_p V_p \frac{d\mathbf{u}_p}{dt} = \rho_f \frac{d}{dt} \left(\int_{V_p} \mathbf{u} dV \right) - \rho_f \sum_{l=1}^{N_l} \mathbf{F}_{p,l} \Delta V_l + (\rho_p - \rho_f) V_p \mathbf{g} + \mathbf{F}_{p,lub} + \mathbf{F}_{p,col}, \quad (5)$$

$$\mathbf{I}_p \frac{d\boldsymbol{\omega}_p}{dt} = \rho_f \frac{d}{dt} \left(\int_{V_p} \mathbf{r} \times \mathbf{u} dV \right) - \rho_f \sum_{l=1}^{N_l} (\mathbf{r}_l \times \mathbf{F}_{p,l}) \Delta V_l + \mathbf{T}_{p,col}, \quad (6)$$

where N_l is the number of Lagrangian grid points, $F_{p,l}$ is the volume force on the Lagrangian grid point calculated by equation (B.3) of the IB method, and $\Delta V_l = \pi \Delta x (12R_p^2 + \Delta x^2) / (3N_l)$ is the volume of a Lagrangian grid cell (Uhlmann, 2005). The discretization schemes for these governing equations are given in Appendix B with details. According to the approximation of the hydrodynamic force (Kempe and Fröhlich, 2012a; Costa et al., 2015; Biegert et al., 2017), the hydrodynamic force is excluded during contact for particles with the Stokes number $St = \rho_p u_{in} D_p / (9\rho_f \nu_f) \geq 5$, where u_{in} is the particle impact velocity.

2.2. Lubrication force

When particles are close to colliding in particle-resolved simulations, the evaluation of the forces acting on a particle can be performed as follows (Breugem, 2010; Kempe and Fröhlich, 2012a; Costa et al., 2015; Biegert et al., 2017): (a) when $\varepsilon \geq \varepsilon_{\Delta x}$, the IB method or a similar approach can be directly used to calculate the hydrodynamic force on the particle, where $\varepsilon = \delta_n / R_p$ is the non-dimensional gap width, δ_n is the distance between two surfaces in a collision, R_p is particle radius, and $\varepsilon_{\Delta x}$ is a predefined constant. (b) When $0 \leq \varepsilon < \varepsilon_{\Delta x}$, the IB method or a similar approach may underpredict the

hydrodynamic force due to a lack of spatial grid resolution. As a remedy, a lubrication model based on asymptotic expansions of analytical solutions for the lubrication force in the Stokes regime can be employed (Brenner, 1961; Cox and Brenner, 1967; Cooley and O’Neill, 1969). (c) When $\varepsilon < 0$, the collision model takes control of the particle, and the hydrodynamic force is neglected. It should be noted that neglecting the hydrodynamic force during a collision is a model assumption.

When a particle approaches another particle or a wall with a finite relative velocity, fluid is squeezed out of the gap and the lubrication model can be employed to calculate the hydrodynamic force with the Stokes flow assumption (Brenner, 1961; Cox and Brenner, 1967; Cooley and O’Neill, 1969). The total lubrication force $\mathbf{F}_{p,lub}$ acting on the particle p can be computed as follows:

$$\mathbf{F}_{p,lub} = \sum_{p,q \neq p}^{N_p} \mathbf{F}_{n,pq}^{lub} + \mathbf{F}_{n,pw}^{lub}, \quad (7)$$

where \mathbf{F}_n^{lub} is the normal lubrication force for a collision pair, N_p is the total particle number, the subscript n indicates the normal direction, and the subscripts pq and pw indicate the contact of particle p with particle q and the wall, respectively. Here, \mathbf{F}_n^{lub} is calculated by the following the two-parameter lubrication model proposed by Breugem (2010) and Costa et al. (2015):

$$\mathbf{F}_n^{lub} = \begin{cases} -6\pi\mu_f R_p \mathbf{u}_{cp,n} (\lambda(\varepsilon) - \lambda(\varepsilon_{\Delta x})), & \varepsilon_\sigma \leq \varepsilon < \varepsilon_{\Delta x} \\ -6\pi\mu_f R_p \mathbf{u}_{cp,n} (\lambda(\varepsilon_\sigma) - \lambda(\varepsilon_{\Delta x})), & 0 \leq \varepsilon < \varepsilon_\sigma \\ 0, & \text{otherwise} \end{cases}, \quad (8)$$

$$\lambda_{pq}(\varepsilon) = \frac{1}{2\varepsilon} - \frac{9}{20} \ln \varepsilon - \frac{3}{56} \varepsilon \ln \varepsilon + O(1), \quad (9)$$

$$\lambda_{pw}(\varepsilon) = \frac{1}{\varepsilon} - \frac{1}{5} \ln \varepsilon - \frac{1}{21} \varepsilon \ln \varepsilon + O(1), \quad (10)$$

where $\mathbf{u}_{cp,n}$ is the normal component of the relative velocity, as defined in Appendix A; λ_{pq} and λ_{pw} are the Stokes amplification factors for the lubrication force in the interactions between particle p and particle q and between particle p and the wall, respectively; $\varepsilon_{\Delta x}$ is the non-dimensional gap spacing related to the grid size (*i.e.*, $D_p/\Delta x$); ε_σ is a fixed minimum gap spacing related to asperities. Following Costa et al. (2015), we adopted $\varepsilon_{\Delta x,pw} = 0.075$, $\varepsilon_{\Delta x,pq} = 0.025$ for $D_p/\Delta x = 20$ and $\varepsilon_{\Delta x,pw} = 0.05$, $\varepsilon_{\Delta x,pq} = 0.025$ for

$D_p/\Delta x = 30$. In addition, $\varepsilon_{\sigma,pw} = 0.0008$ and $\varepsilon_{\sigma,pp} = 0.0001$ were calibrated by matching the trajectories of the particle–wall and particle–particle collisions with the experimental data of [Gondret et al. \(2002\)](#) in the present study. These trajectories are shown in Section 4.1.

2.3. Collision force

The total collision force $\mathbf{F}_{p,col}$ and total torque $\mathbf{T}_{p,col}$ acting on particle p are computed as follows:

$$\mathbf{F}_{p,col} = \sum_{p,q \neq p}^{N_p} (\mathbf{F}_{n,pq}^{col} + \mathbf{F}_{t,pq}^{col}) + \mathbf{F}_{n,pw}^{col} + \mathbf{F}_{t,pw}^{col}, \quad (11)$$

$$\mathbf{T}_{p,col} = \sum_{p,q \neq p}^{N_p} R_p \mathbf{n}_{pq} \times \mathbf{F}_{t,pq}^{col} + R_p \mathbf{n}_{pw} \times \mathbf{F}_{t,pw}^{col}, \quad (12)$$

where \mathbf{F}^{col} is the collision force for a collision pair, \mathbf{n} is the normal unit vector of the contact, and the subscripts n and t indicate the normal and tangential directions, respectively. The collision force \mathbf{F}^{col} is calculated by the soft-sphere model. The model is composed of a linear spring–dashpot system in the normal direction, and a linear spring–dashpot system with a Coulomb friction slider in the tangential direction ([Costa et al., 2015](#)). The normal collision force \mathbf{F}_n^{col} and the tangential collision force \mathbf{F}_t^{col} are determined by

$$\mathbf{F}_n^{col} = -k_n |\delta_n| \mathbf{n} - d_n \mathbf{u}_{cp,n}, \quad (13)$$

$$\mathbf{F}_t^{col} = -k_t \boldsymbol{\delta}_t - d_t \mathbf{u}_{cp,t}, \quad (14)$$

where k_n and k_t are the stiffnesses in the normal and tangential directions, respectively; d_n and d_t are the damping coefficients in the normal and tangential directions, respectively; δ_n is the distance between two surfaces; $\boldsymbol{\delta}_t$ and $\mathbf{u}_{cp,t}$ are the tangential displacement of the spring and the tangential component of the relative velocity, respectively, as defined in Appendix A.

The stiffness and damping coefficients can be derived by the collision time and the restitution coefficient ([Costa et al., 2015](#)), as

$$k_n = \frac{m_{e,n} (\pi^2 + \ln^2 e_{n,d})}{T_c}, \quad d_n = -\frac{2m_{e,n} \ln e_{n,d}}{T_c}, \quad (15)$$

$$k_t = \frac{m_{e,t} (\pi^2 + \ln^2 e_{t,d})}{T_c}, \quad d_t = -\frac{2m_{e,t} \ln e_{t,d}}{T_c}, \quad (16)$$

where $m_{e,n} = (m_p^{-1} + m_q^{-1})^{-1}$ and $m_{e,t} = (1 + 1/K^2)^{-1}m_{e,n}$ are the reduced masses of the linear spring-dashpot system; m_p and m_q are the masses of particles p and q , respectively; K is the normalized particle radius of gyration with $K^2 = 2/5$ for a homogeneous spherical particle; $e_{n,d}$ and $e_{t,d}$ are the dry coefficients of restitution in the normal and tangential directions, respectively.

The stretching collision time model determines the stiffness and damping coefficients through a nonphysical stretched collision time T_c , significantly reducing the stiffness and damping coefficients. To avoid introducing the stretched collision time, the physical collision time should be used (Li et al., 2020). The physical collision time T_c can be calculated by the physical properties of particle as (Zenit et al., 1997)

$$T_c = 7.894 \left(\frac{m_p^2}{E^{*2} u_{in} D_p} \right)^{1/5}, \quad (17)$$

where E^* is the equivalent elasticity of the collision system depending on Young's modulus E and Poisson's ratio ν , which is expressed as follows:

$$\frac{1}{E^*} = \frac{1}{\pi} \left(\frac{1 + \nu_p^2}{E_p} + \frac{1 + \nu_q^2}{E_q} \right). \quad (18)$$

In the present study, we use $E = 200$ GPa and $\nu = 0.3$ for steel particles and $E = 55$ GPa and $\nu = 0.25$ for glass particles. The ratio between T_c and the particle response time $\tau_p = \rho_p D_p^2 / 18\mu_f$ is $O(10^{-4} \sim 10^{-3})$ for 10-mm steel/glass particles with $St = 100$ impacting in air or water, respectively.

When $|\mathbf{F}_t^{col}| \geq \mu_c |\mathbf{F}_n^{col}|$ (μ_c is the friction coefficient), a particle starts to slide. The tangential force is controlled by the slider in the tangential direction based on the Coulomb friction law instead of the tangential displacement, as

$$\mathbf{F}_t^{col} = \mu_c |\mathbf{F}_n^{col}| \mathbf{t}. \quad (19)$$

where \mathbf{t} is the unit vector in the tangential direction. The tangential displacement needs to be reset in order to comply with Coulomb's friction law, which is

$$\delta_t = -\frac{\mu_c |\mathbf{F}_n^{col}| \mathbf{t} + d_t \mathbf{u}_{cp,t}}{k_t}. \quad (20)$$

3. The multiple-time-step integration algorithm (MTSA)

3.1. The motivation

The mismatch problem of the characteristic time scales between particle collision and fluid flow is crucial for particle-resolved simulations. In fact, the

characteristic time scales for fluid flow, fluid-particle interaction and particle collision are quite different in magnitude. We have estimated that the particle collision time can be 3 or 4 orders of magnitude smaller than the particle response time, and thus 1 or 2 orders of magnitude smaller than the flow time scale with $St \sim O(100)$. Using a very fine fluid flow time step Δt_f to resolve particle collision can lead to a highly expensive computation. When employing a single large time step in a particle-resolved simulation, the error of the soft-sphere model is also large and mainly comes from two aspects. First, the particle motion cannot be well resolved by a large flow time step during a collision. It will result in an excessive overlap between colliding surfaces and overpredicting the rebounding trajectory, as shown in figure 1 of [Kempe and Fröhlich \(2012a\)](#). Second, particle velocity rapidly changes during a collision. The surrounding fluid can hardly follow this rapid change with a large flow time step. It may cause an overestimation of the hydrodynamic force by the IB method and underpredicts the rebounding trajectory, as shown in figure 8 of [Costa et al. \(2015\)](#). These two facts prevent the usage of the traditional soft-sphere model with a single large time step. On the other hand, as we have discussed in the introduction, artificially reducing particle stiffness like the SCTA is nonphysical and may also bring in errors in simulations ([Xia et al., 2020](#)).

Due to the aforementioned drawbacks of the existing methods, we propose the MTSA employing a normal fluid flow time step while inserting additional two-level time substeps to resolve fluid-particle interaction and particle motion during a collision, so that the prediction errors by increasing particle stiffness can be significantly reduced and the computation efficiency is not degraded too much at the same time.

3.2. The computation procedure

The MTSA was activated once particle-particle/wall collision happens. A single time step Δt is replaced by three different time steps, namely a fluid flow time step Δt_f and additional two-level time substeps (*i.e.*, fluid-particle interaction time substep Δt_i and particle motion time substep Δt_p) hierarchically inserted into it. As shown in figure 1, $\Delta t_f = T_c/R_f$ is employed to advance fluid flow, $\Delta t_i = T_c/R_i$ to advance fluid-particle interaction, and $\Delta t_p = T_c/R_m$ to advance particle motion. Here, R_f , R_i and R_m are the iteration numbers of fluid flow, fluid-particle interaction and particle motion substeps in one collision time T_c , respectively. Based on the above three parameters, $N_i = R_i/R_f$ and $N_m = R_m/R_f$ can be defined as the iteration

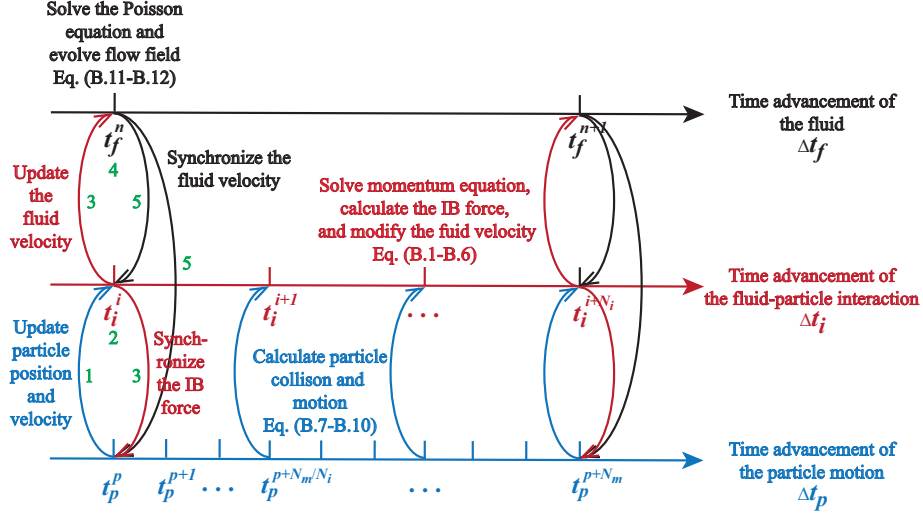


Figure 1: Sketch of the multiple-time-step integration algorithm (MTSA).

numbers of fluid-particle interaction and particle motion substeps in one fluid flow time step. It should be noted that N_i and N_m should be integers, which restrict the choices for R_i and R_m .

The pressure Poisson equation is only solved at the fluid flow step $t = t_f$, which greatly improves the computational efficiency of the MTSA. Local pressure is assumed to be a constant at the fluid-particle interaction and particle motion substeps in a fluid flow step. At a fluid-particle interaction substep $t = t_i$, we solve the flow momentum equation, calculate the IB force, and modify the fluid velocity by the IB force accordingly. At a particle motion substep $t = t_p$, we calculate particle collision and motion. When the time is advanced to the same instant, the information of the fluid flow and particle will be updated and synchronized. The updating and synchronizing process are demonstrated by the arrow lines in figure 1. Particularly, when $t = t_f = t_i = t_p$, the particle position and velocity at $t = t_p$ are updated to the particle-fluid interaction substep before calculating the IB force. Second, the IB force is calculated and used to modify the fluid velocity at $t = t_i$. Third, the calculated IB force at $t = t_i$ is synchronized to the fluid flow step as the input for particle motion, and the modified fluid velocity at $t = t_i$ is also updated as the input for the Poisson equation. Fourth, the Poisson equation and flow field at $t = t_f$ are solved and updated. Finally, the updated fluid velocity at $t = t_f$ is synchronized to $t = t_i$ and $t = t_p$ as the input for

the flow momentum equation and particle motion. When $t \neq t_f$, we only update the particle position and velocity.

In the MTSA, an explicit second-order Runge–Kutta (RK2) method is used for the temporal advancement of the fluid flow (Yang et al., 2017, 2018; Cui et al., 2018; He et al., 2022; Zhu et al., 2022). At each substep of the RK2 method, the fractional-step method of Kim and Moin (1985) is applied to ensure that the flow field is divergence-free. In order to insert enough substeps to ensure that the flow can adapt to the change of particle motion during collisions and reduce the computational cost, the explicit Euler method is adopted in the particle-fluid interaction and particle-motion substeps for time advancement. The discretized equations are presented in Appendix B.

3.3. The advantages

In summary, the proposed MTSA has the following advantages:

(1) Compared with the traditional soft-sphere model, the MTSA significantly improves computational efficiency as it employs a large fluid flow time step Δt_f . The pressure Poisson equation is only solved at the fluid flow time step $t = t_f$, which greatly saves the computation cost. The computational time of the MTSA can be reduced to about one order of magnitude less than that of the traditional soft-sphere model with almost the same accuracy, which will be shown in §4.

(2) Compared with the SCTA, the MTSA employs physical particle stiffness without reducing particle stiffness. It is expected that the problem of hydrodynamic force underestimation will be alleviated or resolved by the MTSA, and the simulation of sediment transport will not be affected by nonphysically reduced particle stiffness. In addition, the parameters R_i in the MTSA has very good universality for different fluid time steps, which will also be shown in §4.

In addition to the aforementioned algorithms proposed in particle-resolved simulations, some numerical algorithms have also been proposed in point particle simulations to address the mismatch of the time scales between particle collision and the fluid flow (Deen et al., 2007; Capecelatro and Desjardins, 2013; Finn et al., 2016). They generally employed two-time scales, where a large time step was adopted to advance fluid flow and the inter-phase coupling, while a small time step was employed for particle motion. Some researchers even used a smaller time scale to calculate particle collisions (Darmana et al., 2006; Marshall, 2009). However, as will be shown in §4,

these algorithms are ineffective in particle-resolved simulations, since fluid-particle interaction is not resolved during a collision.

4. Results

In this section, the accuracy and convergence of the traditional soft-sphere model and the MTSA are assessed through simulations of particle-wall and particle-particle collisions. Furthermore, we discuss the impact of R_f and R_i on the prediction results using the MTSA. Finally, a sediment transport case with thousands of finite-size particles is simulated as a practical application of the MTSA and a demonstration of the difference between the MTSA and the SCTA. [It should be noted that a version of SCTA similar to Costa et al. \(2015\) is adopted here to be compared with the MTSA, which incorporates a two-parameter lubrication model, a linear spring-dashpot system, and substeps for particle collisions and motions.](#)

Because the hydrodynamic force is neglected in a particle collision, which is totally governed by the spring-dashpot system, R_m is not influenced by the grid size and St . We directly determine R_m by normal dry particle-wall and particle-particle collision cases. The simulation results of the restitution coefficient e_n were compared with a given $e_{n,d} = 0.97$ for steel and glass particles. For both $R_m = 40$ and 80, it is found that the relative error between e_n and $e_{n,d}$ is less than 0.1%, which is sufficiently small. Therefore, the impact of R_m is not studied in this section. And $R_m = 40$ is used in the following cases, and $R_m = 80$ is only used when $R_i = 16$.

4.1. Accuracy and convergence of the traditional soft-sphere model

Cases REF, S1 and S2 in table 1 are designed to verify the accuracy and convergence of the traditional soft-sphere model as the benchmark result. These three cases can be regarded as using the MTSA without the fluid-particle interaction substep (*i.e.*, $N_i = R_i/R_f = 1$), which is similar to the algorithm proposed for the point-particle simulations ([Deen et al., 2007](#)). Therefore, there are only two-time steps in cases REF, S1 and S2. Particularly, the Navier-Stokes and fluid-particle interaction equations are solved with the flow time step Δt_f , while the Newton-Euler equations are advanced with the particle motion time step Δt_p . Case REF is regarded as the benchmark case. In case S1, Δt_f was smaller than that in case REF, which is used to verify the accuracy and convergence of case REF. In case S2, Δt_f is larger than that in case REF, which is used to compare with the results of

the MTSA with the same Δt_f to demonstrate the improvement by inserting additional fluid-particle interaction substeps.

Table 1: The MTSA parameters R_f , R_i , and R_m used in different cases of particle-wall and particle-particle collisions. $N_i = R_i/R_f = 1$ indicates that the traditional soft-sphere model is used without the fluid-particle interaction (FPI) substep.

Case	R_f	R_i	R_m	Notes
REF	8	8	40	Benchmark case
S1	16	16	80	Reduce Δt_f , without FPI substep
S2	2	2	40	Increase Δt_f , without FPI substep
MTSA	0.5,1,2	2,4,8,16	40,80	With FPI substep

First, the bouncing motion of a single particle in a viscous fluid with different St and $D_p/\Delta x$ values were simulated to assess the accuracy and convergence of the traditional soft-sphere model in particle-wall collisions. The physical parameters in the simulation were comparable to the experiment of [Gondret et al. \(2002\)](#): $\rho_p = 7800 \text{ kg/m}^3$ and $e_{n,d} = 0.97$, and other parameters are listed in table 2. The computational domain was $12.8D_p \times 25.6D_p \times 12.8D_p$. Two grid resolutions, $D_p/\Delta x = 20$ and $D_p/\Delta x = 30$, were implemented in this simulation. A periodic boundary condition was imposed in the horizontal directions, and a no-slip boundary condition was imposed on both the top and bottom surfaces. A particle was initially placed at $x = L_x/2$, $y = L_y - 0.75D_p$, and $z = L_z/2$. The falling velocity was prescribed following [Biegert et al. \(2017\)](#), where it accelerated smoothly and u_{in} matched the Stokes number in the previously reported experiment ([Gondret et al., 2002](#)) before the collision, as

$$u_p(t) = u_{in} (e^{-40t} - 1), \quad \text{if } \delta_n > R_p. \quad (21)$$

Once the particle reached a distance of $\delta_n = R_p$, we turned off the prescribed velocity. Then, the particle moved under hydrodynamic, gravitational, buoyant, and collision forces. The normal coefficient of restitution is defined as $e_n = u_{out}^*/u_{in}^*$. Following [Costa et al. \(2015\)](#), u_{in}^* and u_{out}^* are defined at the instants $t - t_c = \mp f_s^{-1}$, where t_c is the instant of collision and f_s is the sampling frequency in measurements, which is 500 Hz in the experiment of particle-wall collision ([Joseph et al., 2001](#)) and 100 Hz in the experiment of particle-particle collision ([Yang and Hunt, 2006](#)).

Table 2: Parameters used in the simulation of particle-wall collisions.

St	D_p (mm)	ρ_f (kg/m ³)	μ_f (cP)	u_{in} (m/s)	T_c (s)
6	3	965	100	0.231	2.3×10^{-5}
15	6	965	100	0.288	4.4×10^{-5}
27	6	965	100	0.519	3.9×10^{-5}
60	3	953	20	0.462	2.0×10^{-5}
100	4	953	20	0.577	2.6×10^{-5}
152	3	935	10	0.585	1.9×10^{-5}
193	6	953	20	0.742	3.6×10^{-5}
742	5	920	5	0.856	3.0×10^{-5}

The resulting normal coefficients of restitution e_n are compared with the experimental data of [Joseph et al. \(2001\)](#) and [Gondret et al. \(2002\)](#) here. The simulation results of the coefficient of restitution e_n for normal particle-wall collisions by the traditional soft-sphere model are shown in figure 2. The resulting e_n of case REF agrees well with the experimental results over the entire range of the particle Stokes number. This verifies the accuracy of the traditional soft-sphere model. The resulting e_n values are almost the same when refining the grid (*i.e.*, $D_p/\Delta x = 30$) at $St = 15, 27, 152, 742$ or refining the flow time step Δt_f (*i.e.*, case S1) at $St = 27, 152$. This verifies the convergence of the traditional soft-sphere model. However, e_n is evidently underestimated with a much larger Δt_f (case S2). This is because Δt_f is too large to resolve the fluid-particle interaction so that the surrounding fluid cannot follow the rapid change of the particle velocity during the collision, and the velocity difference between the particle and fluid after the collision is increased. This leads to an overestimation of the hydrodynamic force by the IB method. The underestimated e_n in case S2 can cause a remarkable discrepancy in the particle bouncing trajectories, as shown in figure 3. It is seen that the trajectory of case S1 is almost the same as that of case REF, because the values of e_n are close in the two cases. The trajectory of the refined grid (*i.e.*, $D_p/\Delta x = 30$) is not shown here, as the corresponding e_n and trajectory are very close to those of cases REF and S1.

Next, a moving particle colliding with a steady particle in a viscous fluid with different St and $D_p/\Delta x$ values was simulated to assess the accuracy and convergence of the traditional soft-sphere model in particle-particle collisions. The physical parameters in the simulations were comparable to the

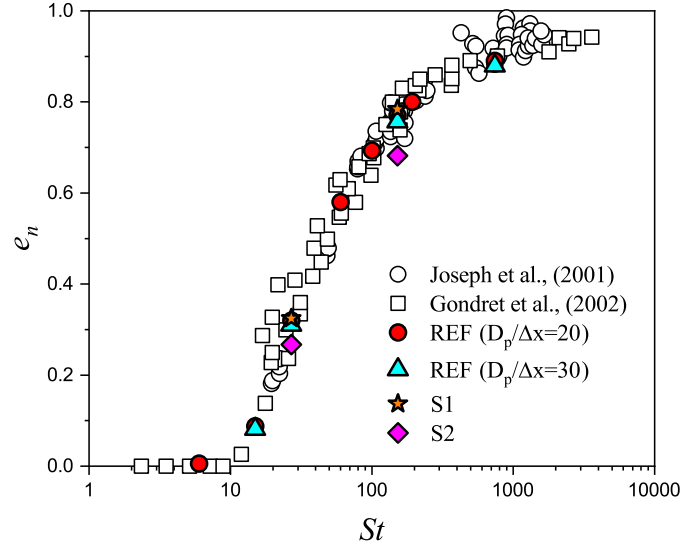


Figure 2: Wet coefficient of restitution for normal particle-wall collisions by the traditional soft-sphere model.

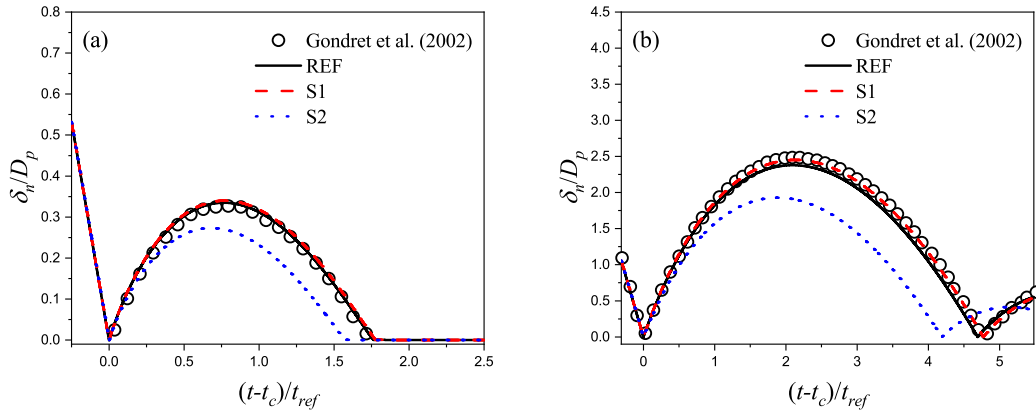


Figure 3: Comparison of the particle trajectories between the experiment and the simulation results by the traditional soft-sphere model with different Stokes numbers and time steps: (a) $St = 27$ and (b) $St = 152$. $t_c = t |_{\delta_n=0}$ is the instant of collision and $t_{ref} = \sqrt{D_p/|g|}$ is the reference time scale.

experiments of [Yang and Hunt \(2006\)](#): $D_p = 12.7$ mm, $\rho_p = 7780$ kg/m³, $\rho_f = 1125$ kg/m³, $\mu_f = 45$ cP and $e_{n,d} = 0.97$, and other parameters are listed in table 3. The computational domain was $6D_p \times 24D_p \times 6D_p$. Two grid resolutions of $D_p/\Delta x = 20$ and 30 were implemented in the simulations. The periodic boundary conditions were applied in all three directions. The steady and moving particles were initially placed at $y = 19D_p$ and $2D_p$, respectively, centered at $x = L_x/2$ and $z = L_z/2$. The velocity of the moving particle was prescribed by the negative form of equation (21) since it was moving upward. The gravitational and buoyancy forces were not considered.

Table 3: Parameters used in the simulation of particle-particle collisions.

St	u_{in} (m/s ⁻¹)	T_c (s)
12.7	0.059	1.3×10^{-4}
21.5	0.099	1.2×10^{-4}
34.3	0.158	1.1×10^{-4}
52.7	0.243	9.6×10^{-5}
135.2	0.623	8.0×10^{-5}
345	1.591	6.6×10^{-5}

In figure 4 (a), the resulting normal coefficients of restitution e_n in the particle-particle collisions are compared with the experimental data of [Yang and Hunt \(2006\)](#) and the numerical results of [Costa et al. \(2015\)](#). The conclusions for the particle-particle collisions are similar to those for particle-wall collisions. The resulting e_n of case REF agrees well with the experimental and numerical results over the entire range of the Stokes number St . The resulting e_n is almost unchanged by refining the grid ($D_p/\Delta x = 30$) at $St = 12, 34, 135, 345$ or reducing the flow time step Δt_f (case S1) at $St = 34$, which verifies the accuracy and convergence of the traditional soft-sphere model. Although the resulting e_n by increasing Δt_f (case S2) is within the range of the widely scattered experimental results, there still was a visible deviation compared with the results of case REF due to the insufficient temporal resolution for fluid-particle interactions. Figure 4 (b) further shows the contact point trajectories of particles at $St = 34$. The trajectories in cases REF and S1 have good agreement with those of [Costa et al. \(2015\)](#). It is seen that the underestimated e_n of case S2 causes a visible discrepancy in the trajectories of the contact point compared with case REF.

The results of the particle-wall and particle-particle collisions indicate

that the traditional soft sphere model can be used to reproduce experimental results only if the flow time step Δt_f is sufficiently small, and increasing Δt_f would result in an underestimation of e_n and non-negligible errors in the particle trajectories. However, the computational cost of using such a small Δt_f is quite high in particle-resolved simulations with a large number of particles. Hence, the MTSA can be a good method to reduce the computational cost of the traditional soft-sphere model while maintaining its accuracy. In the following, the results of case REF will be employed as a benchmark to test the accuracy of the MTSA.

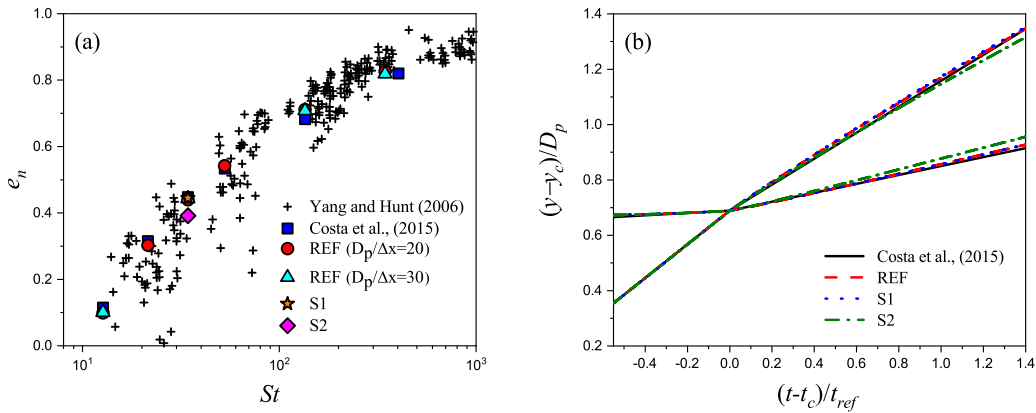


Figure 4: Simulation results of the particle-particle collisions by the traditional soft-sphere model: (a) wet coefficient of restitution in normal particle-particle collisions and (b) trajectories of particle contact points at $St = 34$. $t_c = t |_{\delta_n=0}$ is the instant of collision, and $t_{ref} = \sqrt{D_p/|g|}$ is the reference time scale.

4.2. Assessment of the MTSA

Based on the above results that a large flow time step Δt_f cannot be used to resolve fluid-particle interaction during a collision, we employ a large Δt_f for fluid flow advancement while inserting additional time substeps for fluid-particle interaction in the MTSA. In this subsection, we investigate the influence of the substep iteration number on the simulation results with different particle Stokes number St and grid resolution $D_p/\Delta x$.

4.2.1. Particle-wall collision

For particle-wall collision, we use the same simulation setup and parameters as in §4.1. The resulting normal coefficient of restitution e_n using the

MTSA is compared with that of case REF. Figure 5 shows the error of e_n between the MTSA and case REF with different St and $D_p/\Delta x$ values. The left and right columns show the errors with grid resolutions of $D_p/\Delta x = 20$ and $D_p/\Delta x = 30$, respectively. The dashed line corresponds to zero error.

It can be seen that the general trends of the error curves with R_i in each subfigure are similar in figures 5 (a)-(f). As discussed before, e_n is underestimated ($e_{n,MTSA} - e_{n,REF} < 0$) without including additional fluid-particle interaction substeps, since the fluid flow surrounding the particle cannot adapt to the rapid change of the particle velocity. Therefore, the error curves are mostly under the zero-error line at small R_i values. If more fluid-particle interaction substeps are inserted (increasing R_i), the absolute value of $e_{n,MTSA} - e_{n,REF}$ decreases first. However, as the pressure Poisson equation is not solved in the particle-fluid interaction substeps, the intermediate flow velocities are nonphysical, which leads to an overestimation of e_n at larger R_i values. Therefore, the overall trend of the absolute error of $e_{n,MTSA} - e_{n,REF}$ decreases first then increases with R_i , as shown in figures 5 (a)-(f).

We can elucidate the increase in the error of $e_{n,MTSA} - e_{n,REF}$ with R_i as follows. Based on the Navier-Stokes equations discretized by the explicit Euler method, the intermediate flow velocities at the i th fluid-particle interaction substep during a collision can be expressed as

$$\mathbf{u}^i = \mathbf{u}^{i-1} + \Delta t_i \left(\mathbf{H}^{i-1} + \mathbf{f}^{i-1} - \frac{1}{\rho_f} \nabla p^{i-1} \right), \quad (22)$$

$$\tilde{\mathbf{u}}^i = \tilde{\mathbf{u}}^{i-1} + \Delta t_i \left(\tilde{\mathbf{H}}^{i-1} + \tilde{\mathbf{f}}^{i-1} \right), \quad (23)$$

where \mathbf{u} and $\tilde{\mathbf{u}}$ are the physical (by solving the pressure Poisson equation) and nonphysical (without solving the pressure Poisson equation) intermediate flow velocities, respectively; \mathbf{H} and $\tilde{\mathbf{H}}$ are the sums of the convective and viscous terms with physical and nonphysical intermediate flow velocities, respectively; \mathbf{f} and $\tilde{\mathbf{f}}$ are the volume forces with physical and nonphysical intermediate flow velocities, respectively. Assuming that the initial flow velocity before a collision is \mathbf{u}^0 , the flow velocity after the collision ($i = R_i$) can be expressed as

$$\mathbf{u}^{R_i} = \mathbf{u}^0 + \sum_{i=1}^{R_i} \Delta t_i \left(\mathbf{H}^{i-1} + \mathbf{f}^{i-1} - \frac{1}{\rho_f} \nabla p^{i-1} \right), \quad (24)$$

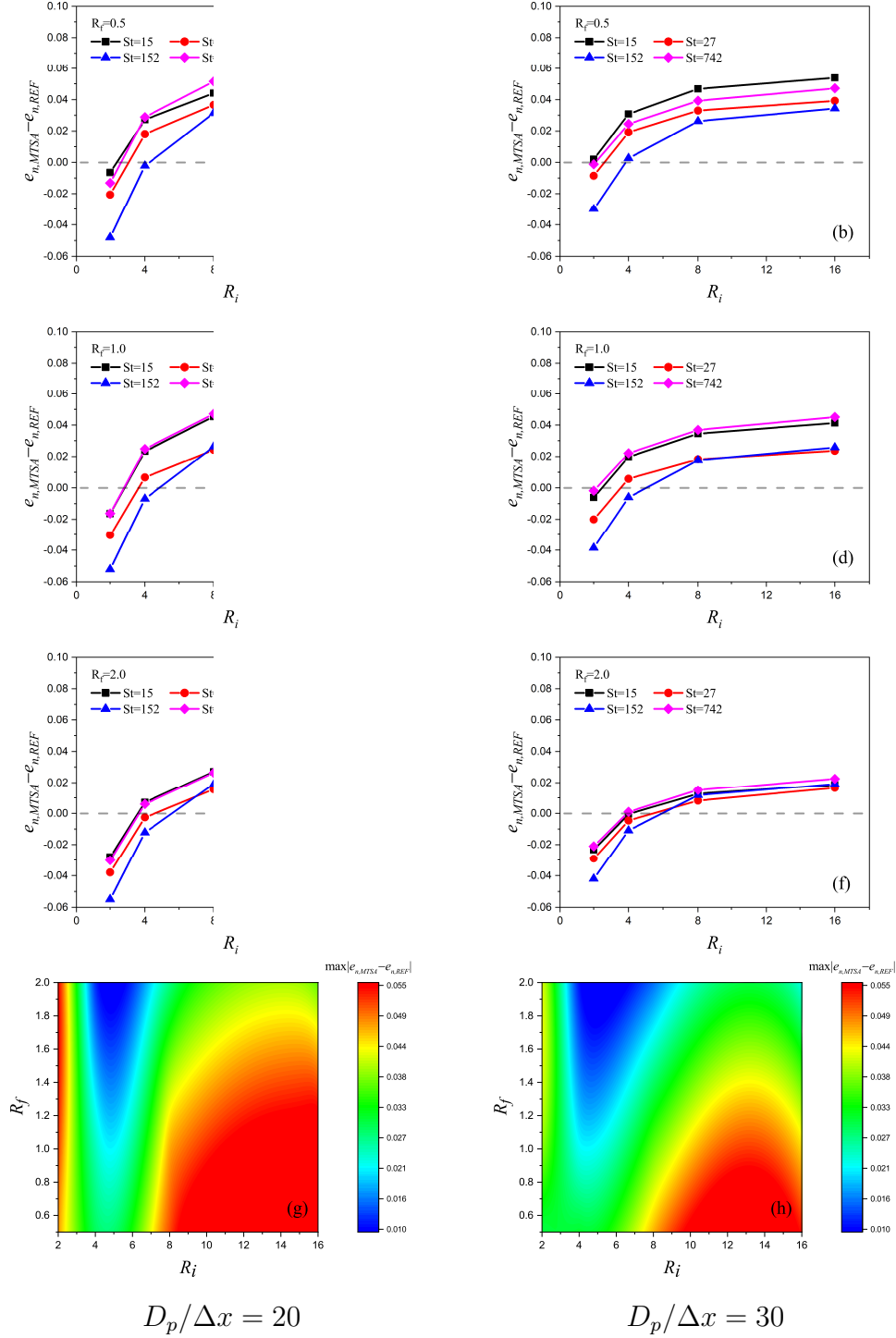


Figure 5: Prediction error of the normal coefficient of restitution e_n between the MTSA and case REF in particle-wall collisions: (a,b) $R_f = 0.5$, (c,d) $R_f = 1.0$, (e,f) $R_f = 2.0$, and (g,h) the contours of the maximum error $|e_{n,MTSA} - e_{n,REF}|$ with $St = 15, 27, 152, 742$.

(a,c,d,g) $D_p/\Delta x = 20$ and (b,d,f,h) $D_p/\Delta x = 30$. The dashed line corresponds to zero error.

$$\tilde{\mathbf{u}}^{R_i} = \mathbf{u}^0 + \sum_{i=1}^{R_i} \Delta t_i \left(\widetilde{\mathbf{H}}^{i-1} + \tilde{\mathbf{f}}^{i-1} \right). \quad (25)$$

The quantities at Eulerian grid points can be transferred to Lagrangian grid points through a regularized Dirac delta function δ_d (Roma et al., 1999). The flow velocity on the particle surface after the collision is

$$\mathbf{U}_l^{R_i} = \mathbf{U}_l^0 + \sum_{i=1}^{R_i} \Delta t_i \left(\mathbf{H}_l^{i-1} + \mathbf{F}_{p,l}^{i-1} - \frac{1}{\rho_f} \nabla P_l^{i-1} \right), \quad (26)$$

$$\tilde{\mathbf{U}}_l^{R_i} = \mathbf{U}_l^0 + \sum_{i=1}^{R_i} \Delta t_i \left(\widetilde{\mathbf{H}}_l^{i-1} + \widetilde{\mathbf{F}}_{p,l}^{i-1} \right), \quad (27)$$

where \mathbf{U}_l , $\mathbf{F}_{p,l}$, \mathbf{H}_l , and P_l are the quantities of \mathbf{u} , \mathbf{f} , \mathbf{H} , and p at Eulerian grid points interpolated at Lagrangian grid points, respectively; and $\tilde{\mathbf{U}}_l$, $\widetilde{\mathbf{F}}_{p,l}$, and $\widetilde{\mathbf{H}}_l$ are the quantities of $\tilde{\mathbf{u}}$, $\tilde{\mathbf{f}}$, and $\widetilde{\mathbf{H}}$ on Eulerian grid points interpolated on Lagrangian grid points, respectively. During a collision, the particle motion is only determined by the collision model and not affected by the fluid flow (Kempe and Fröhlich, 2012a; Costa et al., 2015; Biegert et al., 2017), thus the particle velocities with physical and nonphysical intermediate flow velocities are the same ($\mathbf{U}_p^{R_i} = \tilde{\mathbf{U}}_p^{R_i}$). Based on the IB method as in equation (B.3), the differences in the hydrodynamic force with physical and nonphysical intermediate flow velocities after a collision can be expressed as

$$\begin{aligned} \Delta \mathbf{F}_{p,l}^{R_i} &= \widetilde{\mathbf{F}}_{p,l}^{R_i} - \mathbf{F}_{p,l}^{R_i} \\ &= \frac{\tilde{\mathbf{U}}_p^{R_i} - \mathbf{U}_p^{R_i} + \mathbf{U}_l^{R_i} - \tilde{\mathbf{U}}_l^{R_i}}{\Delta t_i} \\ &= \frac{\mathbf{U}_l^{R_i} - \tilde{\mathbf{U}}_l^{R_i}}{\Delta t_i}. \end{aligned} \quad (28)$$

Substituting equations (26) and (27) into equation (28) yields

$$\Delta \mathbf{F}_{p,l}^{R_i} = \sum_{i=1}^{R_i} \left(\Delta \mathbf{H}_l^{i-1} - \Delta \mathbf{F}_{p,l}^{i-1} - \frac{1}{\rho_f} \nabla P_l^{i-1} \right). \quad (29)$$

Equation (29) includes three terms: $\Delta \mathbf{H}_l^{i-1} = \widetilde{\mathbf{H}}_l^{i-1} - \mathbf{H}_l^{i-1}$, $\Delta \mathbf{F}_{p,l}^{i-1} = \widetilde{\mathbf{F}}_{p,l}^{i-1} - \mathbf{F}_{p,l}^{i-1}$, and ∇P_l^{i-1} , representing the flow velocity error, the hydrodynamic

force error, and the pressure error at each fluid-particle interaction substep, respectively. If $\Delta \mathbf{H}_l^{i-1} - \Delta \mathbf{F}_{p,l}^{i-1} - \nabla P_l^{i-1} / \rho_f \neq 0$, the error of $\Delta \mathbf{F}_{p,l}^{R_i}$ increases as R_i increases, which leads to the error of e_n increasing with R_i . As shown in figures 5 (a-f) and figures 8 (a-f), $e_{n,MTSA}$ increases with R_i , which indicates that the MTSA underestimates the hydrodynamic force as R_i increased and $\Delta \mathbf{H}_l^{i-1} - \Delta \mathbf{F}_{p,l}^{i-1} - \nabla P_l^{i-1} / \rho_f < 0$.

Since insufficient fluid-particle interaction substeps can cause an underestimation of e_n , and too many substeps can cause an overestimation of e_n . Therefore, we may find an optimal value of R_i to minimize the error of e_n . Figures 5 (g) and (h) show the contours of $\max |e_{n,MTSA} - e_{n,REF}|$ for different St and $D_p/\Delta x$ values. It can be found that the maximum error is small for $R_i \in \{4, 5, 6\}$ with different St and $D_p/\Delta x$ values, which indicates that the MTSA has good accuracy with $R_i \in \{4, 5, 6\}$ in the particle-wall collisions. Based on the maximum error in the particle-particle collisions shown in figures 8 (g) and (h), $R_i = 4$ is determined to be the optimal value. The maximum error for $R_i = 4$ is less than 0.031 in the particle-wall collisions, which is small enough.

After determining that $R_i = 4$ is optimal, we employed the MTSA with $R_f = 1, R_i = 4, R_m = 40$ to calculate e_n for particle-wall collisions in the entire range of St . As shown in figure 6, the simulation results of the MTSA agree well with those of case REF and the experimental results over the entire range of St . Therefore, after inserting proper additional fluid-particle interaction substeps, the prediction results by the MTSA are significantly improved compared with those of case S2 in particle-wall collisions. The yellow error bars in figure 6 indicate the prediction uncertainty of e_n with $R_f = 0.5, 1, 2$. The short lengths of the error bars imply that the MTSA has good convergence with these R_f values. A consistent conclusion can be further drawn from the particle trajectories shown in figure 7. It can be seen that the particle trajectories predicted by the MTSA show good agreements with those of case REF, and they are significantly improved compared with those of case S2. The grey area is the particle trajectory range with $R_f = 0.5, 1, 2$. Such small areas demonstrate that the particle trajectories in the particle-wall collisions will not be much affected by Δt_f if it is sufficiently small ($R_f \geq 0.5$).

4.2.2. Particle-particle collision

For particle-particle collisions, we adopted the same simulation setup as that in §4.1. Figure 8 shows the error of the normal coefficient of restitution

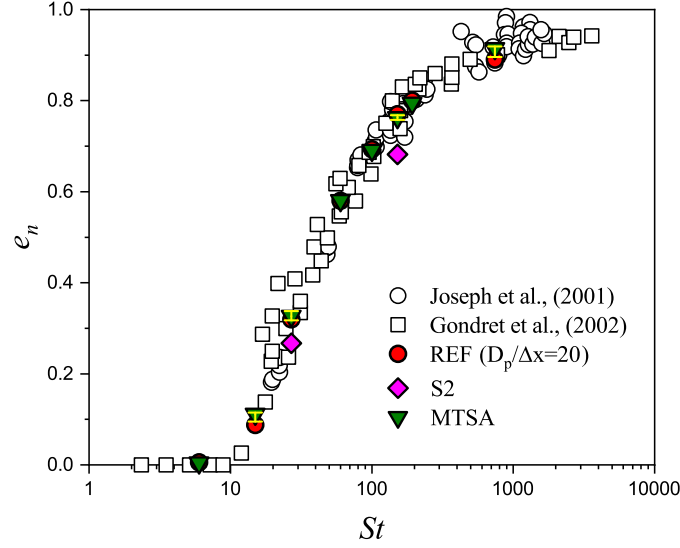


Figure 6: Wet coefficient of restitution in normal particle-wall collisions predicted by the MTSA ($R_f = 1$, $R_i = 4$, $R_m = 40$). The yellow error bar indicates the prediction uncertainty of e_n with $R_f = 0.5, 1, 2$.

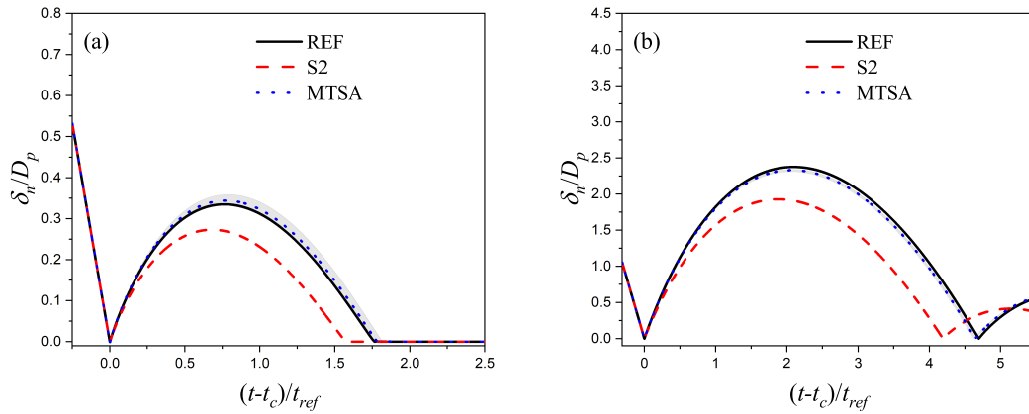


Figure 7: Particle trajectories with different Stokes numbers: (a) $St = 27$ and (b) $St = 152$. The grey area is the particle trajectory range with $R_f = 0.5, 1, 2$. $t_c = t |_{\delta_n=0}$ is the instant of collision, and $t_{ref} = \sqrt{D_p/|g|}$ is the reference time scale.

e_n between the MTSA and case REF. The error curves in each subfigure exhibit the same trend as those in particle-wall collisions, for the same reason as that in particle-wall collisions discussed above.

Figures 8 (g) and (h) show the contours of $\max |e_{n,MTSA} - e_{n,REF}|$ with different St and $D_p/\Delta x$ values. It is seen that the maximum error is small for $R_i \in \{4\}$ with different St and $D_p/\Delta x$ values, which indicates that the MTSA has good accuracy with $R_i = 4$ in particle-particle collisions. Based on the combined results of the particle-wall and particle-particle collisions, $R_i = 4$ is determined to be the optimal value and will be used in the following. The absolute maximum error for $R_i = 4$ is less than 0.024 in the particle-particle collisions, which is also small enough.

We further employed the MTSA with $R_f = 1, R_i = 4, R_m = 40$ to calculate e_n for particle-particle collisions over the entire range of St . As shown in figure 9 (a), the simulation results of the MTSA agree well with those of case REF and the experimental results. Its predictions are much better than those of case S2. The yellow error bars represent the prediction uncertainty of e_n with $R_f = 0.5, 1, 2$. The short lengths of the error bars demonstrate that the MTSA has good convergence with these R_f values. Figure 9 (b) shows the particle trajectories with $St = 34$. The particle trajectories predicted by the MTSA have excellent agreement with those of case REF and are much better than those of case S2. The grey area is the particle trajectory range with $R_f = 0.5, 1, 2$. The small grey areas indicate that the predicted particle trajectories in the particle-particle collisions are not much affected by Δt_f if it is sufficiently small ($R_f \geq 0.5$).

To summarize, by considering the results of particle-wall and particle-particle collisions together, $R_i = 4$ is determined to be optimal for collisions with different St and $D_p/\Delta x$ values. The prediction results by the MTSA with $R_i = 4$ have been shown to be in good agreement with the experimental measurements and the benchmark results (case REF) and made significant improvements over the results without inserting additional fluid-particle interaction substeps (case S2).

4.2.3. Oblique particle-wall collision

Here we assessed the MTSA ($R_f = 1, R_i = 4, R_m = 40$) for oblique particle-wall collisions and compared the results with the experimental data of [Joseph and Hunt \(2004\)](#). The physical parameters in the simulations are close to those in the experiment of [Yang and Hunt \(2006\)](#): $D_p = 2.5$ mm, $\rho_f = 998$ kg/m³, $\mu_f = 1$ cP and $e_{n,d} = 0.97$, and other parameters are listed

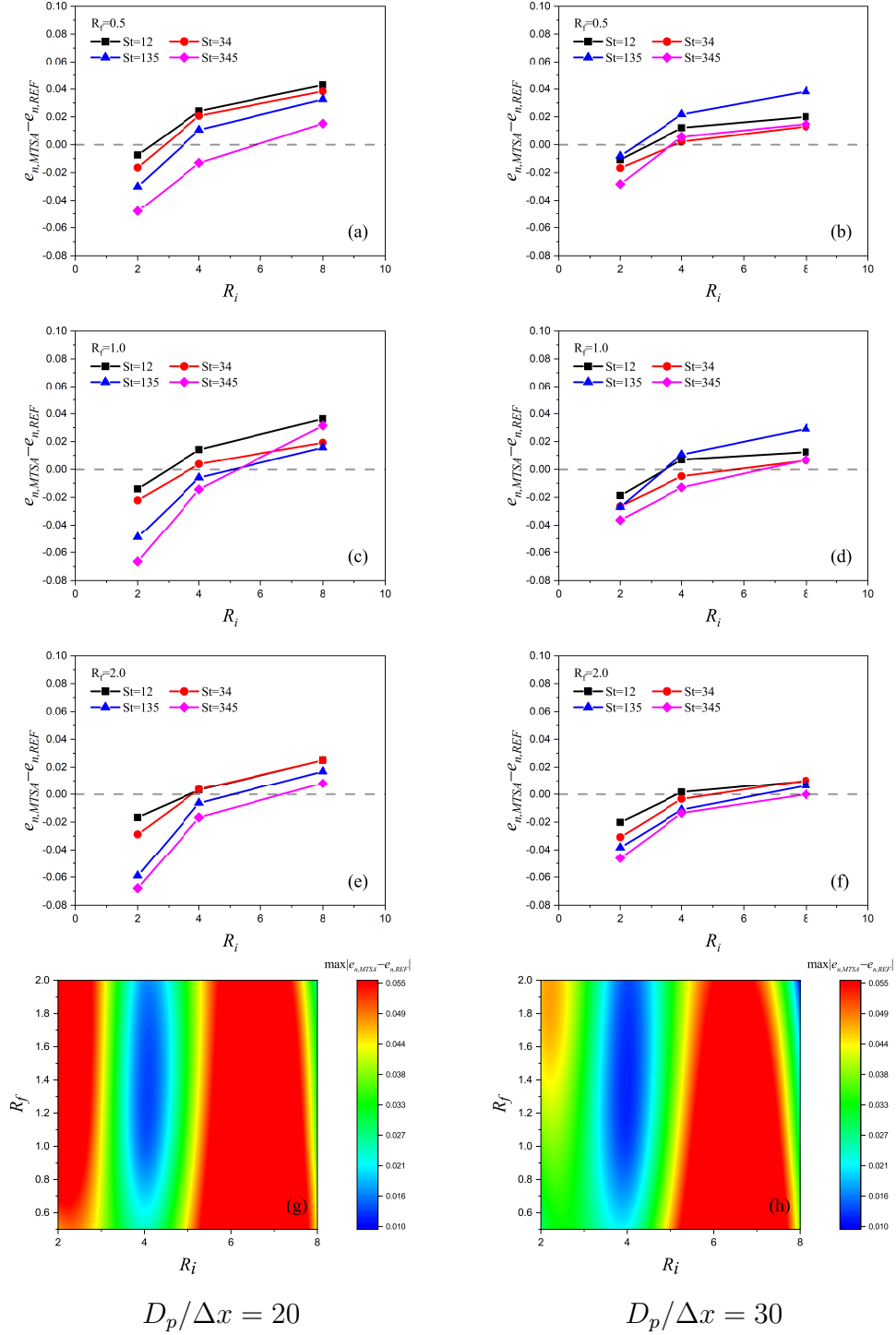


Figure 8: Prediction error of the normal coefficient of restitution e_n between the MTSA and case REF in particle-particle collisions: (a,b) $R_f = 0.5$, (c,d) $R_f = 1.0$, (e,f) $R_f = 2.0$, and (g,h) the contours of the maximum error $|e_{n,MTSA} - e_{n,REF}|$ with $St = 12, 34, 135, 345$.

(a,c,d,g) $D_p/\Delta x = 20$ and (b,d,f,h) $D_p/\Delta x = 30$. The dashed line corresponds to zero error.

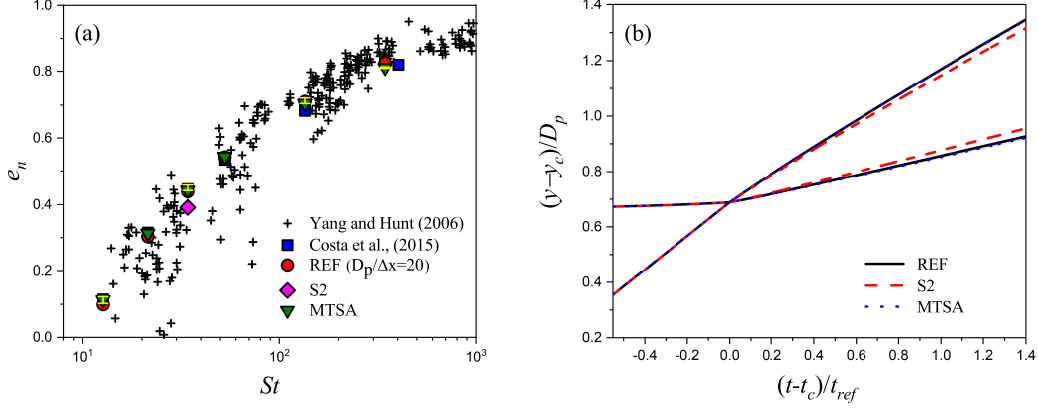


Figure 9: Simulation results of particle-particle collisions by the MTSA: (a) wet coefficient of restitution in normal particle-particle collisions, where the yellow error bars indicate the prediction uncertainty of e_n with $R_f = 0.5, 1, 2$; (b) the predicted trajectories of the particle contact points with $St = 34$, where the grey area is the particle trajectory range with $R_f = 0.5, 1, 2$. $t_c = t |_{\delta_n=0}$ is the instant of collision, and $t_{ref} = \sqrt{D_p/|g|}$ is the reference time scale.

in table 4. The effective angles of incidence and rebounding are defined as $\Psi_{in} = u_{in,t}/u_{in,n}$ and $\Psi_{out} = u_{out,t}/u_{in,n}$, respectively, where $u_{in,n}$ and $u_{in,t}$ are the normal and tangential components of the particle impact velocity, respectively, and $u_{out,t}$ is the tangential component of the particle rebounding velocity. The computational domain and grid resolution are the same as those used for the previous particle-wall collisions in §4.1. Following the work of Costa et al. (2015), the particle falling velocity was controlled by an oblique acceleration with the direction vector $\mathbf{e}_g = -\sin(\phi_{in})\mathbf{e}_y - \cos(\phi_{in})\mathbf{e}_x$ to yield the desired incidence angle Ψ_{in} . The magnitude of the particle acceleration was set to $g = 98.1 \text{ m/s}^2$.

Table 4: Parameters used in the simulation of oblique particle-wall collisions. $\mu_{c,wet}$ is the wet friction coefficient.

Material	ρ_p (kg/m ³)	$e_{n,d}$	$e_{t,d}$	μ_c	$\mu_{c,wet}$
Steel	7800	0.97	0.34	0.11	0.02
Glass	2540	0.97	0.39	0.10	0.15

Comparison of the normalized incidence and the rebounding angle of the

oblique collision between the simulation results obtained by the MTSA and the experimental data for steel and glass particles are presented in figure 10. It is seen that the simulation results by the MTSA are in good agreement with the experimental data of [Joseph and Hunt \(2004\)](#) in the entire range of incidence angles.

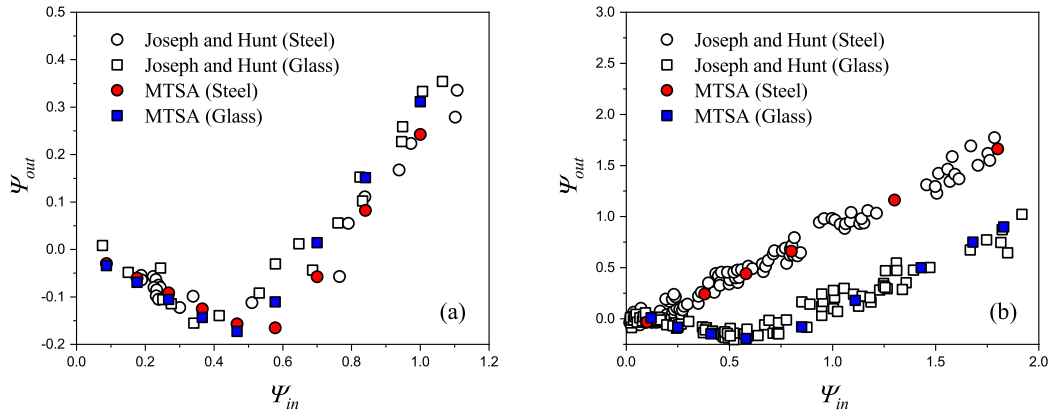


Figure 10: Dependence between the effective angles of the incidence and rebounding: (a) without viscous fluid and (b) with viscous fluid.

4.3. Simulation of turbulent flow over an erodible sediment bed

Now we applied the MTSA with $R_f = 0.5$, $R_i = 4$, $R_m = 40$ to simulate a turbulent flow over an erodible sediment bed. The turbulent flow was driven by a constant pressure gradient that is balanced by the shear stress on the sediment bed. Periodic boundary conditions were imposed in the streamwise and spanwise boundaries of the computational domain, no-slip boundary conditions were applied on the bottom surface of the domain and the particle surfaces, and free-slip boundary conditions were imposed on the top surface of the domain. The sediment bed was laid on the smooth bottom wall of the channel under gravity. The sediment bed consisted of $N_p = 7200$ particles with four layers, as shown in Figure 11. In the present study, the sediment bed was generated by a sedimentation simulation for particles settling under gravity while turning off the hydrodynamic force, similar to [Kidanemariam and Uhlmann \(2014b\)](#).

For the parameters of the carrier phase, the size of the computational domain was $L_x \times L_y \times L_z = (6 \times 1 \times 3)H$ with a uniform Cartesian grid of

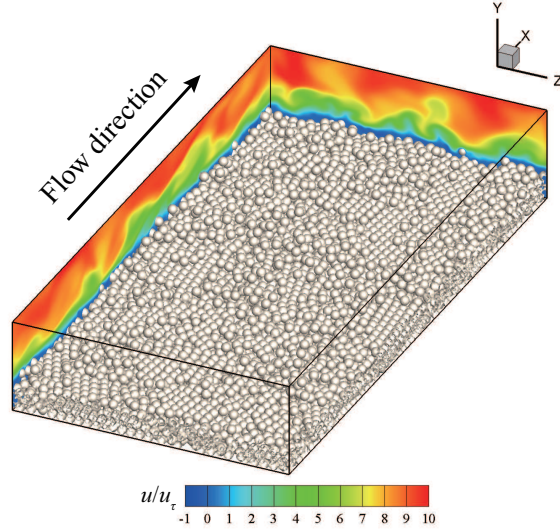


Figure 11: Instantaneous snapshot of the turbulent flow over the erodible sediment bed. The flow field is colored by the value of the non-dimensional streamwise velocity u/u_τ .

$N_x \times N_y \times N_z = 1200 \times 200 \times 600$ grid numbers, where H is the computational domain height in the y direction. Here, x , y , and z denote the streamwise, wall-normal and spanwise directions, respectively. The friction Reynolds number is defined as $Re_\tau = u_\tau H_e / \nu = 94$, where $u_\tau = \sqrt{\tau_b / \rho_f}$ is the friction velocity, τ_b is the mean shear stress at an effective sediment-bed height y_b , and $H_e = H - y_b$ is the effective boundary-layer height. The bulk Reynolds number $Re_b = U_b H_e / \nu$ are 569, 582, and 614, for case MTSA, SCTA1, and SCTA2, respectively, where $U_b = (1/H) \int_0^H \langle u \rangle dy$ is the bulk velocity. The effective bed height y_b was determined at the height where the mean particle porosity $\langle \phi_p \rangle = 0.1$ (Kidānemariam and Uhlmann, 2014a), which yielded $y_b = 0.35H$. The Shields number is $\Theta = u_\tau^2 / ((\rho_p / \rho_f - 1)gD_p) = 0.12$, which is above the critical Shields number $\Theta_c = 0.047$ (Meyer-Peter and Müller, 1948; Wong and Parker, 2006), and the corresponding Galileo number is $Ga = \sqrt{(\rho_p / \rho_f - 1)gD_p^3} / \nu = 42$. The gravitational acceleration is $g = 9.81 \text{ m/s}^2$.

For the parameters of the dispersed phase, the density ratio between the particle and the fluid is $\rho_p / \rho_f = 2.65$. The dimensionless particle diameter is $D_p / H = 0.1$. Referring to the recent particle-resolved sediment transport simulations (Jain et al., 2021; Kidānemariam et al., 2022), the grid resolution was chosen as $D_p / \Delta x = 20$, which is sufficient for sediment transport. The

corresponding Eulerian grid size is $\Delta x^+ = \Delta y^+ = \Delta z^+ = 0.47 < 1$, which is able to fully resolve the turbulent channel flow. The superscript $+$ indicates quantities normalized in viscous units (by u_τ and ν_f). The particle diameter in wall units was $D_p^+ = D_p/(\nu_f/u_\tau) = 14.5$. The mean volume fraction of the dispersed phase was 21%.

For the parameters in the collision model, the normal restitution coefficient is $e_{n,d} = 0.97$, the tangential restitution coefficient is $e_{t,d} = 0.39$, and the friction coefficient is $\mu_c = 0.15$; these were chosen according to the material properties of sand particles (Joseph and Hunt, 2004).

The simulations were carried out on the Tianhe-2A supercomputer with 50 nodes (1200 cores). Each node has two Intel Xeon E5-2692 cores and 64 GB of memory.

4.3.1. Effect of particle stiffness

Cases MTSA, SCTA1, and SCTA2 with different particle stiffness listed in table 5 were designed to investigate the effect of particle stiffness on the turbulence and particle statistics of the sediment transport simulation. For the MTSA, $\Delta t_f = T_{c,min}/R_f = 7.6 \times 10^{-6}$ s was chosen to ensure that it can resolve mostly all collisions with different impact velocities, where $T_{c,min}$ is the minimum physical collision time obtained by equation (17) with the maximum impact velocity $u_{in,max} = 8u_\tau$ based on a similar particle-resolved simulation by Vowinckel et al. (2014). The physical stiffness $E = 55$ GPa for the glass particle was applied in the MTSA, while the particle stiffness was reduced in cases SCTA1 and SCTA2 by stretching the collision time with the stretching coefficient $N = 10$ (Kempe and Fröhlich, 2012a). In case SCTA2, the particle stiffness was further reduced by increasing T_c compared with case SCTA1.

Table 5: Parameters used in the simulations of the turbulent flow over the erodible sediment bed. The CFL number was calculated by $CFL = \max_{i=1,3} |u_i| \Delta t / \Delta x$.

Case	Δt_f (s)	T_c (s)	E (GPa)	CFL	Notes
MTSA	7.6×10^{-6}	Eq.(17)	55	0.113	Benchmark case
SCTA1	7.6×10^{-6}	$10\Delta t_f$	0.03	0.115	Same Δt_f as case MTSA
SCTA2	7.6×10^{-5}	$10\Delta t_f$	10^{-4}	1.21	Same N as case SCTA1

In our simulations, once the volume flux of the turbulent flow was statistically stationary, an averaging procedure described in Appendix C was

applied to the flow and particle variables. In total, 250 snapshots of the flow field and 2500 snapshots of the particles during a time period of $15H/u_\tau$ were collected for time averaging. In order to distinguish whether the error came from reducing particle stiffness or statistical uncertainty, the time period $15H/u_\tau$ was equally divided into two periods of $7.5H/u_\tau$. The results averaged over these two time periods were defined as the lower and upper boundaries (statistical uncertainty range) of the simulation, as shown by the shaded region in figures 12 to 14. The lines/symbols in the following figures are the results averaged over a total time period of $15H/u_\tau$. In the following, the turbulence and particle statistics are compared between cases MTSA, SCTA1 and SCTA2. The wall-normal coordinate $Y = y - y_b$ is adopted and normalized by H_e .

Figure 12 shows the profiles of the mean particle porosity (planar density) obtained in each $x - z$ plane. The operator $\langle \cdot \rangle$ indicates an average over $x - z$ plane (not a slab) and time. With this averaging operation, the theoretical maximum limit of particle porosity in dense packing is 0.906 (the largest planar density in the face-centered cubic structure), which is much larger than 0.74 of the largest particle volume fraction in three-dimensional space. Following Kidanemariam and Uhlmann (2014b), the mean particle porosity was calculated by equation (C.4) in Appendix C. The four peaks under the grey line indicate that the sediment bed consists of four layers of particles. The peak heights correspond to the mean center height of each layer of particles (Vowinckel et al., 2014). It should be noted that the particle porosity (Kidanemariam and Uhlmann, 2014b; Vowinckel et al., 2014), which is the particle fraction in the $x - z$ plane rather than the volume fraction (Rao and Capecelatro, 2019), was employed since the particles are larger than the grid. If we chose a y -slab with a height y_s larger than D_p , the mean volume fraction Φ can be calculated through the integration of the particle porosity as $\Phi = (1/y_s) \int_{y_0}^{y_0+y_s} \langle \phi_p \rangle dy$, where y_0 is the lower boundary of the y -slab. The mean volume fraction of the entire sediment bed is 0.58 with $y_0 = -y_b/H_e$ and $y_s = y_b/H_e$ in the present simulation, which is lower than the theoretical maximum limit of dense packing of 0.74 (Rao and Capecelatro, 2019). The maximum particle porosity is 0.832, which is also lower than the theoretical maximum limit of 0.906 for dense packing. As shown in figure 12, the particle porosity above $Y/H_e = 0.15$ is approximately 0.01, which indicates that particles seldom jumped above $Y/H_e = 0.15$. Therefore, particle samples above $Y/H_e = 0.15$ within the

averaging time window may not be sufficiently large to obtain convergent statistics. This problem can also be seen in figures 9 and 10 of [Ji et al. \(2014\)](#). Therefore, we only focus on the near-wall region ($0 < Y/H_e < 0.15$) in the following analysis.

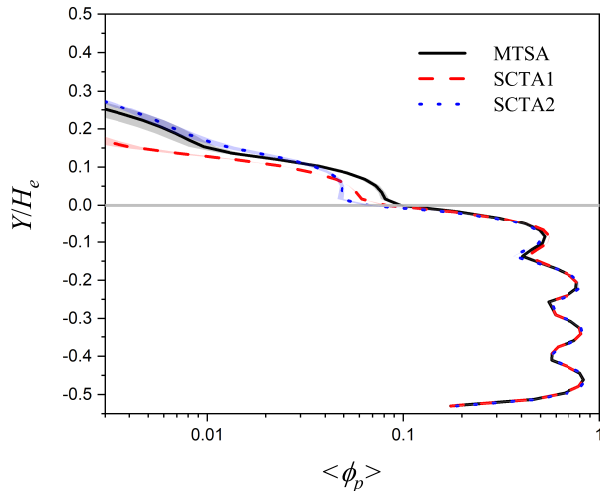


Figure 12: Profiles of the mean particle porosity. The grey line indicates the effective height of the sediment bed. The shaded regions of different colors indicate the ranges of the statistical errors in different cases.

For comparing the present simulation results with available experimental or numerical results, we cannot find any particle-resolved simulation studies or experimental measurements under similar conditions. In many experiments, both the size of particles and the Reynolds number of turbulent flow are much larger than the present one. In addition, as the particle volume fraction is usually very high near a sediment bed, it is very challenging to distinguish tracers and inertial particles in experiment ([Brandt and Coletti, 2022](#)). As a result, near-wall turbulence statistics are almost impossible to be extracted. We cannot find any experimental results of near-sediment-bed turbulence statistics in the literature also. A measurable quantity of sediment transport rate can be compared, which is defined as $q = (\pi D_p^3/6) \left(\sum_{N_p} \langle u_p \rangle \right) / \left(L_x L_y L_z \sqrt{(\rho_p/\rho_f - 1)} \right)$ in a non-dimensional form, where $\langle u_p \rangle$ is mean particle velocity. The non-dimensional sediment transport rates in cases MTSA, SCTA1, and SCTA2 are $q_{MTSA} = 0.0461$, $q_{SCTA1} = 0.0568$, and $q_{SCTA2} = 0.1396$, respectively.

The well-known empirical formula of [Wong and Parker \(2006\)](#) gives $q^* = 4.93 (\theta - \theta_c)^{1.6}$, where θ_c is the critical Shields number. Following [Wong and Parker \(2006\)](#), if $\theta_c = 0.047$ is employed, we can get $q^* = 0.0748$. It seems that the prediction by SCTA1 is the most accurate, but we argue that the formula of [Wong and Parker \(2006\)](#) was fitted with data at much larger flow-submerge ($Y/D_p \sim 40$) and flow Reynolds numbers. The particle stability increases with decreasing flow depth under constant shear velocity, which is likely related to the suppression of the energetic large-scale turbulent motions due to the limited separation between flow depth and roughness length scales (smaller flow Reynolds number) ([Cameron et al., 2020](#)). Therefore, we believe that the actual sediment transport rate under the present simulation condition should be much smaller than $q^* = 0.0748$.

In the near-wall region, the statistical uncertainties of the particle porosity are negligible compared with the errors caused by reducing particle stiffness. The present results show that when particle stiffness is reduced, the mean particle porosity is underestimated, and the underestimation increases as particle stiffness decreased, as displayed in figure 12. The relative difference between the results of case SCTA1 and case MTSA and between case SCTA2 and case MTSA are 24% and 40% at $Y/H_e = 0.02$, respectively. Thus, fewer particles are entrained in cases SCTA1 and SCTA2. This may be caused by excluding the hydrodynamic force during the collisions, which significantly ignores the effect of turbulence on particle entrainment with a time scale smaller than T_c . [Vowinckel et al. \(2016\)](#) found that 96.5% of the entrained particles were triggered by particle collisions. Therefore, the effects of turbulence may be substantially underestimated if T_c is greatly stretched, and fewer particles would be entrained in the near-wall region.

Figure 13 (a) shows the streamwise mean flow velocity profile. In the near-wall region, the statistical uncertainties of the streamwise mean flow velocity are negligible. The results show that when particle stiffness is reduced by the SCTA, the streamwise mean flow velocity is overestimated compared with the MTSA, and the difference increases as particle stiffness decreases. The relative difference between the results of case SCTA1 and case MTSA and the results of case SCTA2 and case MTSA are 6% and 35% at $Y/H_e = 0.02$, respectively. This is probably because fewer particles are entrained from the bed in cases SCTA1 and SCTA2, which exert a smaller drag force on the flow. The profiles of the root-mean-squared (r.m.s) fluctuating flow velocities in the three directions are shown in figure 13 (b). In the near-wall region, it can be seen that the wall-normal and spanwise fluctuating flow velocities are close

between cases SCTA1, SCTA2 and MTSA. For the streamwise fluctuating flow velocity, the statistical uncertainty is smaller than the uncertainty by the collision model. In fact, the r.m.s streamwise fluctuating flow velocity is underestimated by the SCTA compared with the MTSA, and the underestimation increases as particle stiffness decreases. This may be because particles are more difficult to be entrained in cases SCTA1 and SCTA2, which imposes fewer disturbances to the fluid in the near-wall region. Figure 13 (c) shows the profiles of the total shear stress $(-\langle u'v' \rangle + \nu_f d\langle u \rangle / dy) / u_\tau^2$, where u' and v' are the streamwise and wall-normal flow velocity fluctuations, respectively. The total shear stress nicely follows a linear profile in the outer flow indicating that the turbulent flow has been fully developed. The total shear stress is underestimated by the SCTA compared with the MTSA in the near-wall region, and the underestimation increases as particle stiffness decreases.

Figure 14 (a) shows the profiles of the mean particle velocities. It is seen that the profiles of the wall-normal and spanwise mean particle velocities are quite close between cases SCTA1, SCTA2 and MTSA. In the near-wall region, the statistical uncertainties of the streamwise mean particle velocity are much smaller than those by reducing particle stiffness. This result definitely shows that when particle stiffness is artificially reduced, the streamwise mean particle velocity will be overestimated, and the difference increases as particle stiffness decreases. The relative difference of the streamwise mean particle velocity between cases SCTA1 and MTSA and between cases SCTA2 and MTSA can reach up to 87% and 325% at $Y/H_e = 0.02$, respectively. This may be because the mean flow velocity of cases SCTA1 and SCTA2 are higher than that of case MTSA, thus the drag force acting on the entrained particles increases to accelerate particles to higher speeds in cases SCTA1 and SCTA2. Figure 14 (b) displays the profiles of the mean particle angular velocities. It can be seen that the profiles of the streamwise and wall-normal mean particle angular velocities are close between cases SCTA1, SCTA2 and MTSA. In the near-wall region, the statistical uncertainties of the spanwise mean particle angular velocity are much smaller than those by reducing particle stiffness. The results in the near-wall region demonstrate that when particle stiffness is reduced by the SCTA, the spanwise mean particle angular velocity may be overestimated, and the difference increases as particle stiffness decreases. The relative difference of the spanwise mean particle angular velocity between cases SCTA1 and MTSA and between cases SCTA2 and MTSA can reach up to 62% and 150% at $Y/H_e = 0.02$, respectively. This may be because the mean flow velocity gradient is larger in cases SCTA1 and SCTA2.

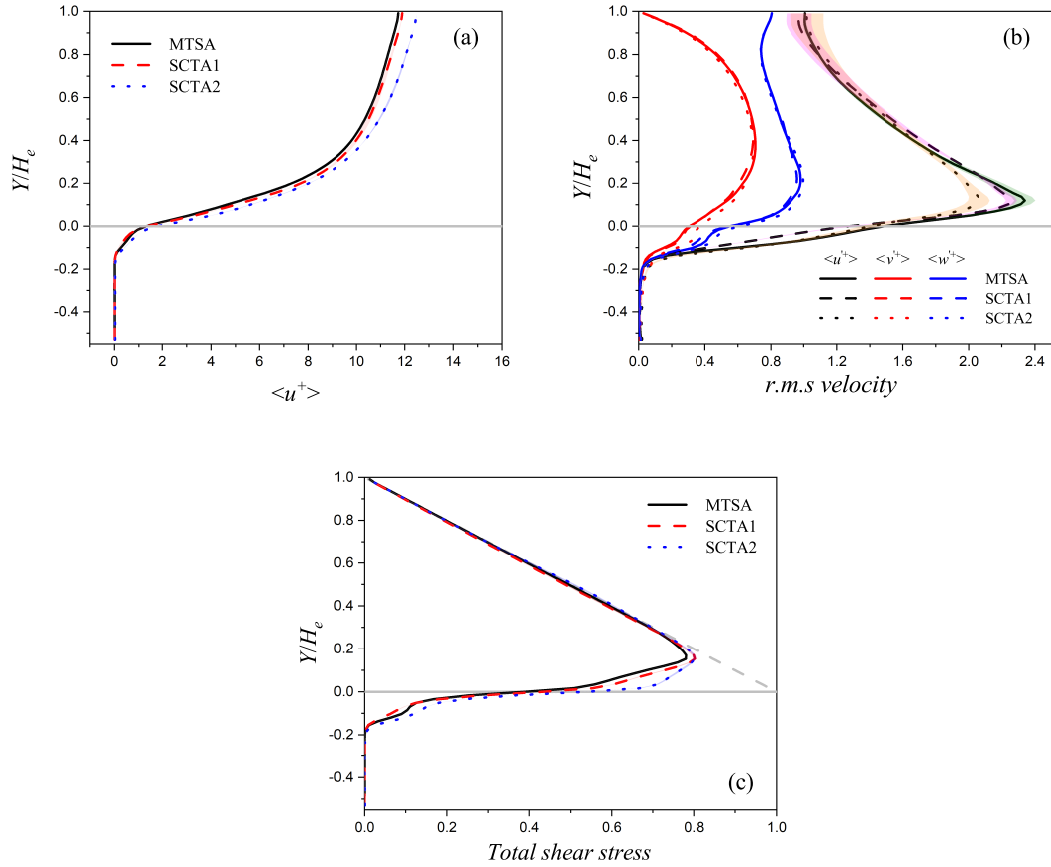


Figure 13: Turbulence statistics in sediment transport simulations: (a) the streamwise mean flow velocity and (b) the root-mean-squared fluctuating flow velocities, and (c) the total shear stress $(-\langle u'v' \rangle + \nu_f d\langle u \rangle/dy)/u_\tau^2$. The grey line indicates the effective height of the sediment bed. The grey dash line indicates $1 - Y/H_e$. The shaded regions indicate the ranges of statistical uncertainties.

It should be noted that a version of SCTA similar to [Costa et al. \(2015\)](#) is adopted here to be compared with the MTSA, which incorporates a two-parameter lubrication model, a linear spring-dashpot system, and substeps for particle collisions and motions. It is found that there are evident differences between the results of the sediment transport case using the SCTA and MTSA for the statistics especially particle statistics if the particle stiffness is greatly reduced. The differences increase as particle stiffness decreases (stretched collision time increases). Using different versions of SCTA with different model details like the lubrication model, linear vs. non-linear spring-dashpot, time integration among others may affect the results. However, we believe that the assumption of excluding the hydrodynamic force during particle collisions and the much longer collision time in the SCTA are the major reasons for the differences between the results using the SCTA and MTSA, as the other modeling and numerical aspects are the same in our code.

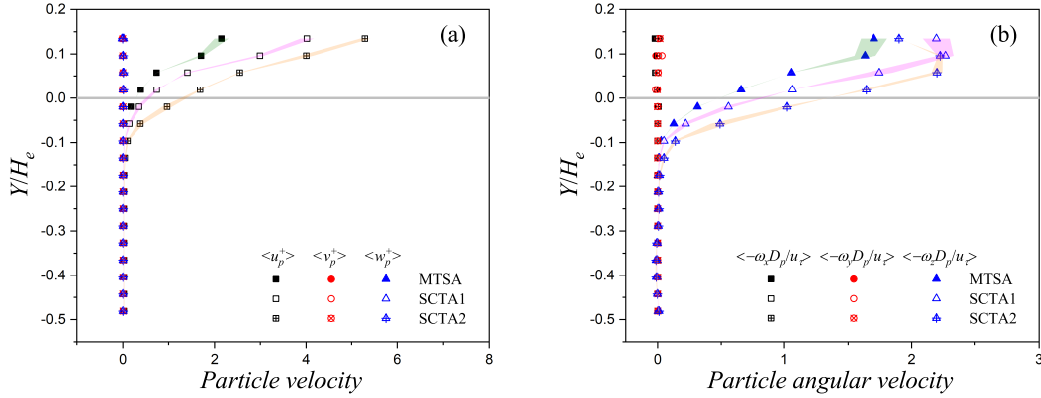


Figure 14: Particle statistics in sediment transport simulations: (a) the mean particle velocity and (b) the mean particle angular velocity. The grey line indicates the effective height of the sediment bed. The shaded regions indicate the ranges of the statistical uncertainties.

4.3.2. The computational cost of the MTSA

The computational cost of a complete simulation of sediment transport using the traditional soft-sphere model with a fine time step is very high. Therefore, we only ran 1000 time steps in case REF to obtain its computation performance. Here we compare the ratio $(T/\Delta t_f)/(T_{REF}/\Delta t_{f,REF})$ between different algorithms, which represents the computational time ratio

for advancing a unit flow time in the simulations, where T is the elapsed clock time spent over 1000 flow time steps. Furthermore, $\Delta t_f/\Delta t_{f,REF} = 16$ (*i.e.*, $R_f = 0.5$) was used in the following simulations, and the computational time ratios of $\Delta t_f/\Delta t_{f,REF} = 4$ and 8 were also tested. As shown in figure 15, the computational time ratio of the MTSA is close to the ideal ratio $\Delta t_{f,REF}/\Delta t_f$. The computational efficiency can be increased by an order of magnitude using the MTSA with $R_f = 0.5$, $R_i = 4$, $R_m = 40$ compared with the traditional soft-sphere model. This is because the pressure Poisson equation is not solved in the inserted substeps, which significantly reduces the computational cost. It is also seen that the computational efficiency of the MTSA is not degraded too much with that of the SCTA.

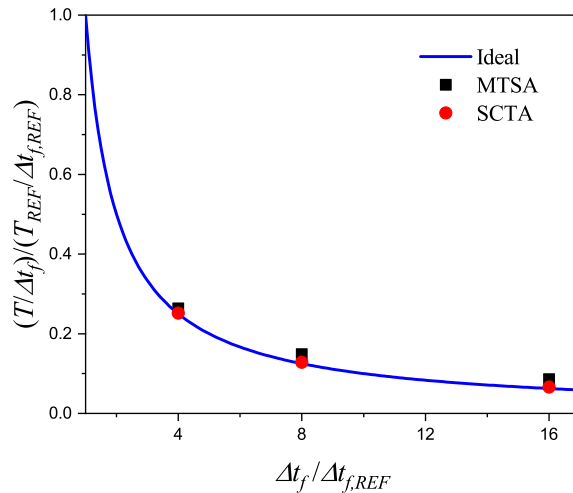


Figure 15: Variation of the computational time ratio with the time step ratio. The blue line is the ideal computational time ratio, which equals $\Delta t_{f,REF}/\Delta t_f$.

5. Conclusions

In the present study, a multiple-time-step integration algorithm (MTSA) has been proposed for particle-resolved simulations with physical collision time. The MTSA adopts three different time steps to resolve fluid flow, fluid-particle interaction and particle collision. We have successfully demonstrated the accuracy and convergence of the MTSA in particle-wall and particle-particle collision problems. It is shown that the MTSA can yield excellent

agreement with experiments and benchmark simulations using the physical collision time and on a coarse grid ($D_p/\Delta x = O(10)$). It also overcomes the main drawback of a version of SCTA similar to [Costa et al. \(2015\)](#), in which an artificially stretched collision time is introduced, which may lead to the collision time being nonphysical and an underestimation of the hydrodynamic force and particle entrainment in sediment transport.

The impact of the parameters R_f , R_i , and R_m in the MTSA has been systematically analyzed and discussed. We found that $R_i = 4$ and $R_m = 40$ are universally suitable for particle-wall and particle-particle collisions over a wide range of particle Stokes numbers. The absolute error of e_n can be controlled to be within about 0.03 for different R_f values. After determining the optimal parameters of the MTSA, we applied the MTSA to simulate a turbulent flow over an erodible sediment bed. The statistics of turbulence and particles by the MTSA and a version of SCTA similar to [Costa et al. \(2015\)](#) were compared to investigate the effect of particle stiffness. The results demonstrated that if particle stiffness is artificially reduced by the SCTA, the number of entrained particles over the erodible sediment bed will be evidently underestimated compared with those by the MTSA, which will mainly impact the streamwise mean flow velocity, streamwise fluctuating flow velocity, streamwise mean particle velocity and spanwise mean particle angular velocity in the near-wall region. The prediction differences increase as particle stiffness decreases. Furthermore, the computation efficiencies between the MTSA and the traditional soft-sphere model were compared. The results indicated that the MTSA can substantially reduce the computational cost by up to one order of magnitude, and make the computational cost acceptable for particle-resolved simulations with physical collision time. As such, the proposed MTSA can be a valuable algorithm for generating high-fidelity and accurate data efficiently in particle-resolved simulations.

For future studies, we plan to perform more intensive particle-resolved simulations of sediment transport, including higher Reynolds numbers and particle/fluid density ratios. For example, the Reynolds number Re_τ is an important non-dimensional parameter that may also affect the prediction difference between the simulations using the SCTA and MTSA, thus simulations at higher Re_τ should be valuable. Simulating sediment transport using the adaptive mesh refinement (AMR) technique to reduce computational costs ([Zeng et al., 2022a,b](#)) is also within our future plans.

6. Acknowledgments

This work was financially supported by grants from the National Natural Science Foundation of China (Nos. 92052202 and 11972175) and the National Numerical Windtunnel project. The computation was performed at the Tianhe-2A supercomputer of the National Supercomputer Center in Guangzhou. The authors report no conflict of interest.

Appendix A. Definitions for particle-particle and particle-wall collision

The variables used in particle collision are defined below. Some definitions depend on whether the interaction is between a particle p and a wall (P-W) or between a particle p and a particle q (P-P). The variables are defined as follows:

\mathbf{n} - normal unit vector of contact

$$\mathbf{n} = \frac{\mathbf{x}_q - \mathbf{x}_p}{|\mathbf{x}_q - \mathbf{x}_p|}, \quad (\text{P-P}), \quad (\text{A.1})$$

$$\mathbf{n} = \frac{\mathbf{x}_w - \mathbf{x}_p}{|\mathbf{x}_w - \mathbf{x}_p|}, \quad (\text{P-W}), \quad (\text{A.2})$$

δ_n - distance between two surfaces

$$\delta_n = |\mathbf{x}_q - \mathbf{x}_p| - R_p - R_q, \quad (\text{P-P}), \quad (\text{A.3})$$

$$\delta_n = |\mathbf{x}_w - \mathbf{x}_p| - R_p, \quad (\text{P-W}), \quad (\text{A.4})$$

\mathbf{u}_{cp} - relative velocity of contact point

$$\mathbf{u}_{cp} = \mathbf{u}_p - \mathbf{u}_q + R_p \boldsymbol{\omega}_p \times \mathbf{n} + R_q \boldsymbol{\omega}_q \times \mathbf{n}, \quad (\text{P-P}), \quad (\text{A.5})$$

$$\mathbf{u}_{cp} = \mathbf{u}_p + R_p \boldsymbol{\omega}_p \times \mathbf{n}, \quad (\text{P-W}), \quad (\text{A.6})$$

$\mathbf{u}_{cp,n}$ - normal component of \mathbf{u}_{cp}

$$\mathbf{u}_{cp,n} = (\mathbf{u}_{cp} \cdot \mathbf{n}) \mathbf{n}, \quad (\text{A.7})$$

$\mathbf{u}_{cp,t}$ - tangential component of \mathbf{u}_{cp}

$$\mathbf{u}_{cp,t} = \mathbf{u}_{cp} - \mathbf{u}_{cp,n}, \quad (\text{A.8})$$

and $\boldsymbol{\delta}_t$ is the tangential displacement of the contact point.

The direction of the tangential unit vector changes in every time step. Therefore, we need to rotate the displacement from the previous time step onto a plane tangent to \mathbf{n} . Then $\boldsymbol{\delta}_t$ is calculated to be the same as [Biegert et al. \(2017\)](#):

$$\tilde{\boldsymbol{\delta}}_t = \boldsymbol{\delta}_t^{k-1} - (\boldsymbol{\delta}_t^{k-1} \cdot \mathbf{n})\mathbf{n}, \quad (\text{A.9})$$

$$\hat{\boldsymbol{\delta}}_t = \frac{|\boldsymbol{\delta}_t^{k-1}|}{|\tilde{\boldsymbol{\delta}}_t|} \tilde{\boldsymbol{\delta}}_t, \quad (\text{A.10})$$

$$\boldsymbol{\delta}_t^k = \hat{\boldsymbol{\delta}}_t + \Delta t \mathbf{u}_{cp,t}. \quad (\text{A.11})$$

Appendix B. Discretization schemes

The discretization schemes adopted in the MTSA are as follows: an explicit second-order Runge–Kutta (RK2) method is used for fluid flow advancement ([Yang et al., 2017, 2018](#); [Cui et al., 2018](#); [He et al., 2022](#)). At each substep of the RK2 method, the fractional-step method of [Kim and Moin \(1985\)](#) is applied to ensure that the flow field is divergence-free. In order to insert enough substeps to ensure that the flow can adapt to the change of the particle motion during collisions and reduce the computational cost, the explicit Euler method is adopted in the substeps for time advancement. The fluid and particle are coupled by the multidirect forcing IB method ([Luo et al., 2007](#); [Breugem, 2012](#)). The discretized equations of fluid flow and particle motion in the k th Runge–Kutta step are given as follows:

do $k = 1, 2$

$$\hat{\mathbf{u}}^{k-1,0} = \mathbf{u}^{k-1},$$

do $i = 1, N_i$

$$\hat{\mathbf{u}}^{k-1,i} = \hat{\mathbf{u}}^{k-1,i-1} + \Delta t_i \left[\alpha_k \hat{\mathbf{H}}^{k-1,i-1} - \beta_k \left(\hat{\mathbf{H}}^{k-2,i-1} - \frac{1}{\rho} \nabla p^{k-2} \right) \right], \quad (\text{B.1})$$

$$\mathbf{u}^{*,0} = \hat{\mathbf{u}}^{k-1,i},$$

$$\mathbf{F}_{p,l}^{k-1,i,0} = 0,$$

do $s = 1, N_s$

$$\mathbf{U}_l^{*,s-1} = \sum_{ijk} \mathbf{u}_{ijk}^{*,s-1} \delta_d \left(\mathbf{x}_{ijk} - \mathbf{X}_l^{k-1,i-1,N_m} \right) \Delta x \Delta y \Delta z, \quad (\text{B.2})$$

$$\mathbf{F}_{p,l}^{*,s-1} = \frac{\mathbf{U}_p(\mathbf{X}_l^{k-1,i-1,N_m}) - \mathbf{U}_l^{*,s-1}}{\Delta t_i}, \quad (\text{B.3})$$

$$\mathbf{f}_{ijk}^{*,s-1} = \sum_{l=1}^{N_l} \mathbf{F}_{p,l}^{*,s-1} \delta_d(\mathbf{x}_{ijk} - \mathbf{X}_l^{k-1,i-1,N_m}) \Delta V_l, \quad (\text{B.4})$$

$$\mathbf{u}^{*,s} = \mathbf{u}^{*,s-1} + (\alpha_k - \beta_k) \Delta t_i \mathbf{f}^{*,s-1}, \quad (\text{B.5})$$

$$\mathbf{F}_{p,l}^{k-1,i,s} = \mathbf{F}_{p,l}^{k-1,i,s-1} + (\alpha_k - \beta_k) \mathbf{F}_{p,l}^{*,s-1}, \quad (\text{B.6})$$

enddo

$$\hat{\mathbf{u}}^{k-1,i} = \mathbf{u}^{*,N_s},$$

$$\mathbf{u}_p^{k-1,i,0} = \mathbf{u}_p^{k-1,i-1,N_m},$$

$$\mathbf{x}_p^{k-1,i,0} = \mathbf{x}_p^{k-1,i-1,N_m},$$

$$\boldsymbol{\omega}_p^{k-1,i,0} = \boldsymbol{\omega}_p^{k-1,i-1,N_m},$$

do $p = 1, N_m$

$$\begin{aligned} \mathbf{u}_p^{k-1,i,p} = & \mathbf{u}_p^{k-1,i,p-1} + (\alpha_k - \beta_k) \left\{ -\frac{\Delta t_p \rho_f}{V_p \rho_p} \sum_{l=1}^{N_l} \mathbf{F}_{p,l}^{k-1,i,N_s} \Delta V_l + \right. \\ & \left. \frac{1}{V_p \rho_p} \left(\left\{ \int_{V_p} \mathbf{u} dV \right\}^N - \left\{ \int_{V_p} \mathbf{u} dV \right\}^{N-1} \right) + \Delta t_p \left(1 - \frac{\rho_f}{\rho_p} \right) \mathbf{g} + \right. \\ & \left. \Delta t_p \frac{\mathbf{F}_{p,lub}^{k-1,i,p-1}}{\rho_p V_p} + \Delta t_p \frac{\mathbf{F}_{p,col}^{k-1,i,p-1}}{\rho_p V_p} \right\}, \end{aligned} \quad (\text{B.7})$$

$$\mathbf{x}_p^{k-1,i,p} = \mathbf{x}_p^{k-1,i,p-1} + (\alpha_k - \beta_k) \Delta t_p \mathbf{u}_p^{k-1,i,p}, \quad (\text{B.8})$$

$$\begin{aligned} \boldsymbol{\omega}_p^{k-1,i,p} = & \boldsymbol{\omega}_p^{k-1,i,p-1} + (\alpha_k - \beta_k) \left\{ -\Delta t_p \frac{\rho_f}{I_p} \sum_{l=1}^{N_l} \mathbf{r}_l \times \mathbf{F}_{p,l}^{k-1,i,N_s} \Delta V_l + \right. \\ & \left. \frac{\rho_f}{I_p} \left(\left\{ \int_{V_p} \mathbf{r} \times \mathbf{u} dV \right\}^N - \left\{ \int_{V_p} \mathbf{r} \times \mathbf{u} dV \right\}^{N-1} \right) + \Delta t_p \frac{\mathbf{T}_{p,col}^{k-1,i,p-1}}{I_p} \right\}, \end{aligned} \quad (\text{B.9})$$

enddo

$$\mathbf{U}_p \left(\mathbf{X}_l^{k-1,i,N_m} \right) = \mathbf{u}_p^{k-1,i,N_m} + \boldsymbol{\omega}_p^{k-1,i,N_m} \times \left(\mathbf{X}_l^{k-1,i,N_m} - \mathbf{x}_p^{k-1,i,N_m} \right), \quad (\text{B.10})$$

enddo

$$\nabla^2 p^{k-1} = \frac{\rho_f}{\alpha_k \Delta t_f} \nabla \cdot \hat{\mathbf{u}}^{k-1,N_i}, \quad (\text{B.11})$$

$$\mathbf{u}^k = \hat{\mathbf{u}}^{k-1,N_i} - \frac{\alpha_k \Delta t_f}{\rho_f} \nabla p^{k-1}, \quad (\text{B.12})$$

enddo

where the superscripts N , k , i , p , and s are the indices of the flow time step, the Runge–Kutta substep, the fluid–particle interaction substep, the particle motion substep, and the IB method iteration substep, respectively. The coefficients in the RK2 scheme are $\alpha_1 = 1$, $\beta_1 = 0$, and $\alpha_2 = \beta_2 = 0.5$. N_s is the number of iterations to calculate the IB force in the multidirect forcing immersed boundary method (Luo et al., 2007; Breugem, 2012). The idea of this method is to iteratively determine the IB force to make the fluid velocity modified by the IB force better satisfy the no-slip boundary condition on the particle surface. $N_s = 3$ is employed following the suggestion of Breugem (2012). The subscripts ijk refer to the quantities on an Eulerian grid with indices (i, j, k) , and the subscript l refers to the quantity on a Lagrangian point with index l . $\hat{\mathbf{u}}$ is the fluid velocity in fluid–particle interaction substep, $\hat{\mathbf{H}} = -\nabla \cdot (\hat{\mathbf{u}}\hat{\mathbf{u}}) + \nu_f \nabla^2 \hat{\mathbf{u}}$ is the sum of the convection and viscous terms. \mathbf{u}^* , \mathbf{f}^* and \mathbf{x} are the intermediate fluid velocity, volume force, and coordinate on the Eulerian grid, respectively, and \mathbf{U}^* , \mathbf{F}^* , \mathbf{X} are the corresponding quantities on the Lagrangian grid. The quantities between the Eulerian and Lagrangian grid points are transferred through a regularized Dirac delta function δ_d . Here, we use the three-point regularized Dirac delta function of Roma et al. (1999). The volume integrals $\int_{V_p} \mathbf{u} dV$ and $\int_{V_p} \mathbf{r} \times \mathbf{u} dV$ are numerically calculated according to Kempe and Fröhlich (2012b). ΔV_l is the volume of the Lagrangian grid cell, and \mathbf{U}_p is the velocity on the particle surface.

Appendix C. Averaging for flow and particle variables

C.1. Averaging for flow variables

Before averaging the flow variables, an indicator function needs to be defined as $\phi_f(\mathbf{x}, t)$ to distinguish an Eulerian grid point at a position \mathbf{x}

that is inside or outside of a particle, following [Kidānemariam and Uhlmann \(2014b\)](#), which is

$$\phi_f(\mathbf{x}, t) = \begin{cases} 1, & \text{if } \mathbf{x} \text{ is outside a particle,} \\ 0, & \text{otherwise.} \end{cases} \quad (\text{C.1})$$

Based on the indicator function $\phi_f(\mathbf{x}, t)$, only the flow data outside of the particle are accounted for averaging as follows:

$$n_f(y_j) = \sum_{n=1}^{N_t} \sum_{i=1}^{N_x} \sum_{k=1}^{N_z} \phi_f(\mathbf{x}_{ijk}, t^n), \quad (\text{C.2})$$

where $n_f(y_j)$ is the total number of grids in the $x-z$ plane over N_t time steps for the flow statistics at a given height y_j . Therefore, the ensemble average of the flow variables $\xi_f(\mathbf{x}, t)$ can be defined as

$$\langle \xi_f \rangle (y_j) = \frac{1}{n_f(y_j)} \sum_{n=1}^{N_t} \sum_{i=1}^{N_x} \sum_{k=1}^{N_z} \xi_f(\mathbf{x}_{ijk}, t^n) \phi_f(\mathbf{x}_{ijk}, t^n), \quad (\text{C.3})$$

where the operator $\langle \cdot \rangle$ indicates the average over an $x-z$ plane and time. The particle porosity $\langle \phi_p \rangle (y_j)$ can be deduced from $\phi_f(\mathbf{x}, t)$:

$$\langle \phi_p \rangle (y_j) = \frac{1}{N_t N_x N_z} \sum_{n=1}^{N_t} \sum_{i=1}^{N_x} \sum_{k=1}^{N_z} (1 - \phi_f(\mathbf{x}_{ijk}, t^n)), \quad (\text{C.4})$$

C.2. Averaging for particle variables

Particle variables are averaged over all particles within each slab. A slab is generated by dividing H by a thickness of Δh . An indicator function $\varphi_p^j(y_p, t)$ is defined to distinguish the center height y_p of a particle inside or outside of a slab with index j as follows:

$$\varphi_p^j(y_p, t) = \begin{cases} 1, & \text{if } (j-1)\Delta h \leq y < j\Delta h, \\ 0, & \text{otherwise.} \end{cases} \quad (\text{C.5})$$

Based on the indicator function $\varphi_p^j(y_p, t)$, the particle number in each slab can be calculated as

$$n_p^j = \sum_{n=1}^{N_t} \sum_{l=1}^{N_p} \varphi_p^j(y_p^l, t^n), \quad (\text{C.6})$$

where n_p^j is the total particle number in the j slab over N_t time steps. Therefore, the averaged particle variable ξ_p can be defined as

$$\langle \xi_p(y^j) \rangle = \frac{1}{n_p^j} \sum_{n=1}^{N_t} \sum_{l=1}^{N_p} \varphi_p^j(y_p^l, t^n) \xi_p^l(t^n). \quad (\text{C.7})$$

A slab thickness of $\Delta h = D_p/4$ was selected in the present study.

References

- Akiki, G., Jackson, T., Balachandar, S., 2017. Pairwise interaction extended point-particle model for a random array of monodisperse spheres. *Journal of Fluid Mechanics* 813, 882–928.
- Ardekani, M. N., Costa, P., Breugem, W. P., Brandt, L., 2016. Numerical study of the sedimentation of spheroidal particles. *International Journal of Multiphase Flow* 87, 16–34.
- Bagchi, P., Balachandar, S., 2003. Effect of turbulence on the drag and lift of a particle. *Physics of fluids* 15 (11), 3496–3513.
- Balachandar, S., Eaton, J. K., 2010. Turbulent dispersed multiphase flow. *Annual Review of Fluid Mechanics* 42, 111–133.
- Biegert, E., Vowinckel, B., Meiburg, E., 2017. A collision model for grain-resolving simulations of flows over dense, mobile, polydisperse granular sediment beds. *Journal of Computational Physics* 340, 105–127.
- Brandt, L., Coletti, F., 2022. Particle-laden turbulence: progress and perspectives. *Annual Review of Fluid Mechanics* 54, 159–189.
- Brenner, H., 1961. The slow motion of a sphere through a viscous fluid towards a plane surface. *Chemical Engineering Science* 16 (3-4), 242–251.
- Breugem, W.-P., 2010. A combined soft-sphere collision/immersed boundary method for resolved simulations of particulate flows. In: *Fluids Engineering Division Summer Meeting*. No. FEDSM-ICNMM2010-30634. pp. 2381–2392.

- Breugem, W.-P., 2012. A second-order accurate immersed boundary method for fully resolved simulations of particle-laden flows. *Journal of Computational Physics* 231 (13), 4469–4498.
- Cameron, S., Nikora, V., Witz, M., 2020. Entrainment of sediment particles by very large-scale motions. *Journal of Fluid Mechanics* 888, A7.
- Capecelatro, J., Desjardins, O., 2013. An Euler–Lagrange strategy for simulating particle-laden flows. *Journal of Computational Physics* 238, 1–31.
- Cooley, M., O’Neill, M., 1969. On the slow motion generated in a viscous fluid by the approach of a sphere to a plane wall or stationary sphere. *Mathematika* 16 (1), 37–49.
- Costa, P., Boersma, B. J., Westerweel, J., Breugem, W.-P., 2015. Collision model for fully resolved simulations of flows laden with finite-size particles. *Physical Review E* 92 (5), 053012.
- Costa, P., Brandt, L., Picano, F., 2020. Interface-resolved simulations of small inertial particles in turbulent channel flow. *Journal of Fluid Mechanics* 883, A54.
- Costa, P., Brandt, L., Picano, F., 2021. Near-wall turbulence modulation by small inertial particles. *Journal of Fluid Mechanics* 922, A9.
- Cox, R. G., Brenner, H., 1967. The slow motion of a sphere through a viscous fluid towards a plane surface: small gap widths, including inertial effects. *Chemical Engineering Science* 22 (12), 1753–1777.
- Cui, Z., Yang, Z., Jiang, H.-Z., Huang, W.-X., Shen, L., 2018. A sharp-interface immersed boundary method for simulating incompressible flows with arbitrarily deforming smooth boundaries. *International Journal of Computational Methods* 15 (01), 1750080.
- Darmana, D., Deen, N. G., Kuipers, J., 2006. Parallelization of an Euler–Lagrange model using mixed domain decomposition and a mirror domain technique: Application to dispersed gas–liquid two-phase flow. *Journal of Computational Physics* 220 (1), 216–248.
- Deen, N., Annaland, M. V. S., Van der Hoef, M. A., Kuipers, J., 2007. Review of discrete particle modeling of fluidized beds. *Chemical Engineering Science* 62 (1-2), 28–44.

- Eaton, J. K., 2009. Two-way coupled turbulence simulations of gas-particle flows using point-particle tracking. *International Journal of Multiphase Flow* 35 (9), 792–800.
- Feng, Z.-G., Michaelides, E. E., Mao, S., 2010. A three-dimensional resolved discrete particle method for studying particle-wall collision in a viscous fluid. *Journal of Fluids Engineering* 132 (9), 091302.
- Finn, J. R., Li, M., Apte, S. V., 2016. Particle based modelling and simulation of natural sand dynamics in the wave bottom boundary layer. *Journal of Fluid Mechanics* 796, 340–385.
- Glowinski, R., Pan, T.-W., Hesla, T. I., Joseph, D. D., 1999. A distributed Lagrange multiplier/fictitious domain method for particulate flows. *International Journal of Multiphase Flow* 25 (5), 755–794.
- Glowinski, R., Pan, T.-W., Hesla, T. I., Joseph, D. D., Periaux, J., 2001. A fictitious domain approach to the direct numerical simulation of incompressible viscous flow past moving rigid bodies: application to particulate flow. *Journal of Computational Physics* 169 (2), 363–426.
- Gondret, P., Lance, M., Petit, L., 2002. Bouncing motion of spherical particles in fluids. *Physics of Fluids* 14 (2), 643–652.
- He, S., Yang, Z., Sotiropoulos, F., Shen, L., 2022. Numerical simulation of interaction between multiphase flows and thin flexible structures. *Journal of Computational Physics* 448, 110691.
- Hertz, H., 1882. Über die berührung fester elastischer körper. *Journal für die reine und angewandte Mathematik* 92 (22), 156–171.
- Homann, H., Bec, J., Grauer, R., 2013. Effect of turbulent fluctuations on the drag and lift forces on a towed sphere and its boundary layer. *Journal of Fluid Mechanics* 721, 155–179.
- Huang, W.-X., Tian, F.-B., 2019. Recent trends and progress in the immersed boundary method. *Proceedings of the Institution of Mechanical Engineers, Part C: Journal of Mechanical Engineering Science* 233 (23-24), 7617–7636.
- Izard, E., Bonometti, T., Lacaze, L., 2014. Simulation of an avalanche in a fluid with a soft-sphere/immersed boundary method including a lubrication force. *Journal of Computational Multiphase Flows* 6 (4), 391–406.

- Jain, R., Tschisgale, S., Fröhlich, J., 2019. A collision model for dns with ellipsoidal particles in viscous fluid. *International Journal of Multiphase Flow* 120, 103087.
- Jain, R., Tschisgale, S., Fröhlich, J., 2021. Impact of shape: DNS of sediment transport with non-spherical particles. *Journal of Fluid Mechanics* 916, A38.
- Ji, C., Munjiza, A., Avital, E., Xu, D., Williams, J., 2014. Saltation of particles in turbulent channel flow. *Physical Review E* 89 (5), 052202.
- Joseph, G., Hunt, M., 2004. Oblique particle-wall collisions in a liquid. *Journal of Fluid Mechanics* 510, 71–93.
- Joseph, G., Zenit, R., Hunt, M., Rosenwinkel, A., 2001. Particle-wall collisions in a viscous fluid. *Journal of Fluid Mechanics* 433, 329–346.
- Kempe, T., Fröhlich, J., 2012a. Collision modelling for the interface-resolved simulation of spherical particles in viscous fluids. *Journal of Fluid Mechanics* 709, 445–489.
- Kempe, T., Fröhlich, J., 2012b. An improved immersed boundary method with direct forcing for the simulation of particle laden flows. *Journal of Computational Physics* 231 (9), 3663–3684.
- Kidanemariam, A. G., Scherer, M., Uhlmann, M., 2022. Open-channel flow over evolving subaqueous ripples. *Journal of Fluid Mechanics* 937, A26.
- Kidanemariam, A. G., Uhlmann, M., 2014a. Direct numerical simulation of pattern formation in subaqueous sediment. *Journal of Fluid Mechanics* 750.
- Kidanemariam, A. G., Uhlmann, M., 2014b. Interface-resolved direct numerical simulation of the erosion of a sediment bed sheared by laminar channel flow. *International Journal of Multiphase Flow* 67, 174–188.
- Kim, J., Moin, P., 1985. Application of a fractional-step method to incompressible navier-stokes equations. *Journal of Computational Physics* 59 (2), 308–323.

- Li, Q., Abbas, M., Morris, J. F., 2020. Particle approach to a stagnation point at a wall: Viscous damping and collision dynamics. *Physical Review Fluids* 5 (10), 104301.
- Luo, K., Hu, C., Wu, F., Fan, J., 2017. Direct numerical simulation of turbulent boundary layer with fully resolved particles at low volume fraction. *Physics of Fluids* 29 (5), 053301.
- Luo, K., Wang, Z., Fan, J., Cen, K., 2007. Full-scale solutions to particle-laden flows: Multidirect forcing and immersed boundary method. *Physical Review E* 76 (6), 066709.
- Marshall, J. S., 2009. Discrete-element modeling of particulate aerosol flows. *Journal of Computational Physics* 228 (5), 1541–1561.
- Meyer-Peter, E., Müller, R., 1948. Formulas for bed-load transport. In: IAHSR 2nd Meeting, Stockholm, appendix 2. IAHR.
- Mindlin, R. D., Deresiewicz, H., 1953. Elastic spheres in contact under varying oblique forces. *Journal of Applied Mechanics* 20 (3), 327–344.
- Mittal, R., Iaccarino, G., 2005. Immersed boundary methods. *Annual Review of Fluid Mechanics* 37, 239–261.
- Papista, E., Dimitrakis, D., Yiantsios, S., 2011. Direct numerical simulation of incipient sediment motion and hydraulic conveying. *Industrial & Engineering Chemistry Research* 50 (2), 630–638.
- Peng, C., Ayala, O. M., Wang, L.-P., 2020. Flow modulation by a few fixed spherical particles in a turbulent channel flow. *Journal of Fluid Mechanics* 884, A15.
- Picano, F., Breugem, W.-P., Brandt, L., 2015. Turbulent channel flow of dense suspensions of neutrally buoyant spheres. *Journal of Fluid Mechanics* 764, 463–487.
- Rao, A. A., Capecelatro, J., 2019. Coarse-grained modeling of sheared granular beds. *International Journal of Multiphase Flow* 114, 258–267.
- Ray, S., Kempe, T., Fröhlich, J., 2015. Efficient modelling of particle collisions using a non-linear viscoelastic contact force. *International Journal of Multiphase Flow* 76, 101–110.

- Rettinger, C., Rde, U., 2022. An efficient four-way coupled lattice Boltzmann–discrete element method for fully resolved simulations of particle-laden flows. *Journal of Computational Physics* 453, 110942.
- Roma, A. M., Peskin, C. S., Berger, M. J., 1999. An adaptive version of the immersed boundary method. *Journal of Computational Physics* 153 (2), 509–534.
- Seyed-Ahmadi, A., Wachs, A., 2020. Microstructure-informed probability-driven point-particle model for hydrodynamic forces and torques in particle-laden flows. *Journal of Fluid Mechanics* 900, A21.
- Shao, X., Wu, T., Yu, Z., 2012. Fully resolved numerical simulation of particle-laden turbulent flow in a horizontal channel at a low Reynolds number. *Journal of Fluid Mechanics* 693, 319–344.
- Tao, S., Zhang, H., Guo, Z., Wang, L.-P., 2018. A combined immersed boundary and discrete unified gas kinetic scheme for particle–fluid flows. *Journal of Computational Physics* 375, 498–518.
- Tenneti, S., Subramaniam, S., 2014. Particle-resolved direct numerical simulation for gas-solid flow model development. *Annual Review of Fluid Mechanics* 46, 199–230.
- Tschisgale, S., Kempe, T., Frhlich, J., 2018. A general implicit direct forcing immersed boundary method for rigid particles. *Computers & Fluids* 170, 285–298.
- Uhlmann, M., 2005. An immersed boundary method with direct forcing for the simulation of particulate flows. *Journal of Computational Physics* 209 (2), 448–476.
- Uhlmann, M., 2008. Interface-resolved direct numerical simulation of vertical particulate channel flow in the turbulent regime. *Physics of Fluids* 20 (5), 053305.
- Verzicco, R., 2023. Immersed boundary methods: Historical perspective and future outlook. *Annual Review of Fluid Mechanics* 55, 129–155.
- Vowinkel, B., Jain, R., Kempe, T., Frhlich, J., 2016. Entrainment of single particles in a turbulent open-channel flow: A numerical study. *Journal of Hydraulic Research* 54 (2), 158–171.

- Vowinckel, B., Kempe, T., Fröhlich, J., 2014. Fluid–particle interaction in turbulent open channel flow with fully-resolved mobile beds. *Advances in Water Resources* 72, 32–44.
- Vreman, A., 2016. Particle-resolved direct numerical simulation of homogeneous isotropic turbulence modified by small fixed spheres. *Journal of Fluid Mechanics* 796, 40–85.
- Wang, S., Vanella, M., Balaras, E., 2019. A hydrodynamic stress model for simulating turbulence/particle interactions with immersed boundary methods. *Journal of Computational Physics* 382, 240–263.
- Wang, Y., Zhu, Z., Hu, R., Shen, L., 2022. Direct numerical simulation of a stationary spherical particle in fluctuating inflows. *AIP Advances* 12 (2), 025019.
- Wong, M., Parker, G., 2006. Reanalysis and correction of bed-load relation of Meyer-Peter and Müller using their own database. *Journal of Hydraulic Engineering* 132 (11), 1159–1168.
- Xia, Y., Xiong, H., Yu, Z., Zhu, C., 2020. Effects of the collision model in interface-resolved simulations of particle-laden turbulent channel flows. *Physics of Fluids* 32 (10), 103303.
- Xia, Y., Yu, Z., Lin, Z., Guo, Y., 2022a. Improved modelling of interfacial terms in the second-moment closure for particle-laden flows based on interface-resolved simulation data. *Journal of Fluid Mechanics* 952, A25.
- Xia, Y., Yu, Z., Pan, D., Lin, Z., Guo, Y., 2022b. Drag model from interface-resolved simulations of particle sedimentation in a periodic domain and vertical turbulent channel flows. *Journal of Fluid Mechanics* 944, A25.
- Yang, F.-L., Hunt, M., 2006. Dynamics of particle-particle collisions in a viscous liquid. *Physics of Fluids* 18 (12), 121506.
- Yang, Z., Deng, B.-Q., Shen, L., 2018. Direct numerical simulation of wind turbulence over breaking waves. *Journal of Fluid Mechanics* 850, 120–155.
- Yang, Z., Lu, X.-H., Guo, X., Liu, Y., Shen, L., 2017. Numerical simulation of sediment suspension and transport under plunging breaking waves. *Computers & Fluids* 158, 57–71.

- Yu, Z., Shao, X., 2007. A direct-forcing fictitious domain method for particulate flows. *Journal of Computational Physics* 227 (1), 292–314.
- Yu, Z., Shao, X., 2010. Direct numerical simulation of particulate flows with a fictitious domain method. *International Journal of Multiphase Flow* 36 (2), 127–134.
- Yu, Z., Xia, Y., Guo, Y., Lin, J., 2021. Modulation of turbulence intensity by heavy finite-size particles in upward channel flow. *Journal of Fluid Mechanics* 913, A3.
- Zeng, Y., Bhalla, A. P. S., Shen, L., 2022a. A subcycling/non-subcycling time advancement scheme-based dlm immersed boundary method framework for solving single and multiphase fluid–structure interaction problems on dynamically adaptive grids. *Computers & Fluids* 238, 105358.
- Zeng, Y., Xuan, A., Blaschke, J., Shen, L., 2022b. A parallel cell-centered adaptive level set framework for efficient simulation of two-phase flows with subcycling and non-subcycling. *Journal of Computational Physics* 448, 110740.
- Zenit, R., Hunt, M. L., Brennen, C. E., 1997. Collisional particle pressure measurements in solid-liquid flows. *Journal of Fluid Mechanics* 353, 261–283.
- Zhang, Y., Jiang, M., Chen, X., Yu, Y., Zhou, Q., 2020. Modeling of the filtered drag force in gas–solid flows via a deep learning approach. *Chemical Engineering Science* 225, 115835.
- Zhou, Q., Fan, L.-S., 2014. A second-order accurate immersed boundary-lattice boltzmann method for particle-laden flows. *Journal of Computational Physics* 268, 269–301.
- Zhou, Q., Fan, L.-S., 2015. Direct numerical simulation of low-reynolds-number flow past arrays of rotating spheres. *Journal of Fluid Mechanics* 765, 396–423.
- Zhu, Z., Hu, R., Lei, Y., Shen, L., Zheng, X., 2022. Particle resolved simulation of sediment transport by a hybrid parallel approach. *International Journal of Multiphase Flow* 152, 104072.